Materialia 7 (2019) 100364

Contents lists available at ScienceDirect

Materialia

journal homepage: www.elsevier.com/locate/mtla

Full Length Article

A truncated-Scheil-type model for columnar solidification of binary alloys in the presence of melt convection

M. Torabi Rad*, C. Beckermann

Department of Mechanical Engineering, University of Iowa, Iowa City, IA 52242, USA

ARTICLE INFO

Keywords:
Solidification
Melt convection
Truncated-Scheil
Macrosegregation and channel segregates
Primary dendrite tip undercooling

ABSTRACT

A two-phase truncated-Scheil-type model is developed for columnar solidification of binary alloys in the presence of melt convection and liquid undercooling ahead of the primary dendrite tips. The model is derived from a three-phase model, which takes into account liquid undercooling ahead and behind the primary tips. These models are used to simulate a numerical solidification benchmark problem, and their predictions are compared with those of a Scheil-type model that disregards liquid undercooling and solute diffusion in solid. Simulation results reveal that the predictions of the truncated-Scheil-type and three-phase models are nearly identical, indicating that undercooling behind the primary tips can be disregarded and the truncated-Scheil-type model can replace the significantly more complex three-phase model. The truncated-Scheil-type and three-phase models smoothly recover the Scheil-type model as the value of the dendrite tip selection parameter is increased. Taking into account liquid undercooling changes the melt convection pattern around the columnar front and the form of channel segregates but does not change the overall macrosegregation pattern.

1. Introduction

Solidification of metals and alloys is important in industrial processes such as metal casting, additive manufacturing, and welding. On Earth, where gravity is present, solidification typically occurs in the presence of buoyancy-driven melt convection (i.e., double diffusive natural convection), which is generated due to the dependence of the liquid density on temperature and/or solute concentration in the liquid. Melt convection changes the temperature distribution during solidification and is typically the main reason for the formation of a type of casting defect known as macrosegregation, which refers to solute composition inhomogeneities at the macroscale. In addition, melt convection is the only reason for the formation of a critical casting defect known as channel segregates, which are narrow, pencil-like macrosegregation patterns that are highly enriched by solute elements. Macrosegregation deteriorates the quality of cast products, and the presence of channel segregates might result in rejection of those products. Predicting these defects using computer models is therefore critical for the industry, and this can be achieved only if melt convection is incorporated into computational models.

Incorporating melt convection in macroscopic solidification models to simulate macrosegregation and channel segregates was pioneered by Beckermann and Viskanta [1,2] and Bennon and Incropera [3,4] in the mid-1980s and has since been the subject of numerous studies. For a comprehensive review, the reader is referred to Beckermann [5] and Ludwig et al. [6] and references therein. Most studies have, however, used models that entirely neglect the constitutional undercooling of the liquid, hereafter referred to as liquid undercooling. During solidification, because heat and/or solute diffusion rates are limited, the liquid typically becomes undercooled locally: its local temperature becomes less than the local liquidus temperature corresponding to the local solute concentration in the liquid. Accounting for liquid undercooling is, in general, important because liquid undercooling is the key in determining the position of the primary dendrite tips, and important phenomena such as nucleation of equiaxed grains can be predicted only if liquid undercooling is taken into account. The main reason that neglecting liquid undercooling has been a common assumption in the literature is that models making that assumption have the advantage of a relatively simple numerical implementation, leading to their extensive use in the literature. As examples of recent and highly relevant studies, Carozzani et al. [7] and Saad et al. [8] used such a macroscopic model to simulate solidification in the presence of melt convection in a solidification benchmark experiment and during directional solidification of indium 75 wt. pct. gallium, respectively. Kumar et al. [9,10] used a similar model to investigate the effects of the mesh size, numerical treatment of the permeability term in the liquid momentum equation, and the inclusion of the inertia term in that equation on the predicted macrosegregation and channel segregates. Bellet et al. [11] proposed a numerical

* Corresponding author. Access e.V., Intzestraße 5, D-52072, Aachen, Germany.
E-mail addresses: m.torabirad@access.rwth-aachen.de, mtorabirad@uiowa.edu (M. Torabi Rad).

https://doi.org/10.1016/j.mtla.2019.100364
Received 25 March 2019; Accepted 25 May 2019
Available online 29 May 2019

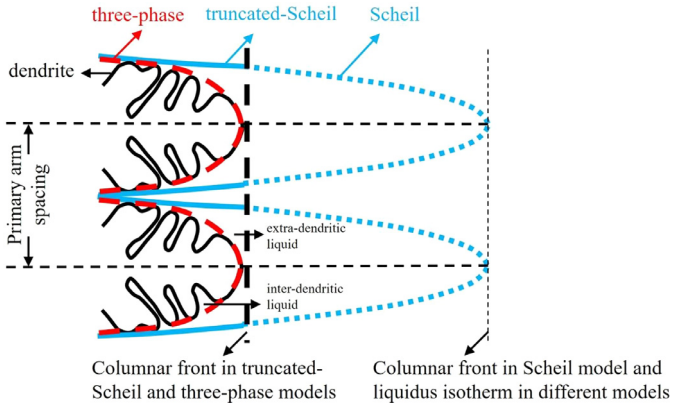

Fig. 1. A schematic of two adjacent columnar dendrites (black) and their shape approximated in the Scheil (dotted blue), truncated-Scheil (solid blue), and three-phase models (red).(For interpretation of the references to color in this figure legend, the reader is referred to the web version of this article.)

benchmark problem for solidification of binary alloys in the presence of melt convection. Combeau et al. [12] compared the predictions of the different computer codes for that benchmark problem. Again, these studies have all disregarded liquid undercooling.

To account for liquid undercooling in macroscale solidification models, Flood and Hunt [13] introduced the so-called truncated-Scheil model. The term Scheil, in that paper and this one, is used to refer to models that account for neither solute diffusion in solid nor liquid undercooling. Fig. 1 shows a schematic of two adjacent columnar dendrites (black), hereafter referred to as dendrites, and their shape approximated in the Scheil (dotted blue) and truncated-Scheil (solid blue) models. In both models, the liquidus isotherm (thin vertical dashed line) is at the same position. In the Scheil model, the primary tips of the dendrites are located at the liquidus isotherm; therefore, in that model, solidification starts at the liquidus temperature. In the truncated-Scheil model, however, the primary tips of the dendrites are located at a distance behind the liquidus isotherm, and the imaginary surface that connects them is termed the columnar front (i.e., the thick vertical dashed line). Note that, behind the columnar front, the shape of the dendrites in the Scheil and truncated-Scheil models are identical. In other words, by truncating the dendrites of the Scheil model at the position of the columnar front, one gets the dendrites of the truncated-Scheil model. The truncated-Scheil model accounts for liquid undercooling because the liquid between the columnar front and the liquidus isotherm is undercooled. In that model, the growth velocity of the tips, and therefore the velocity of the columnar front, is linked to the liquid undercooling ahead of the columnar front through a dendrite tip growth model. In summary, Flood and Hunt's truncated-Scheil model [13], is a macroscale model that allows incorporation of liquid undercooling ahead of the columnar primary tips but disregards melt convection.

In the literature, macroscale models that incorporate both liquid undercooling and melt convection are available. These models are typically based on the multiphase modeling framework developed in the pioneering and widely-accepted work of Wang and Beckermann [14], which allows one to develop macroscale models that incorporate microscale and mesoscale phenomena. For the details of the framework, the reader is referred to the original paper [14]. In brief, as shown in Fig. 1, models based on this framework consist of three phases: solid, inter-dendritic liquid, and extra-dendritic liquid. The two liquid phases are separated by the dendritic envelope (or grain envelope), which is a smooth, virtual surface that connects the primary tips to the tips of actively growing secondary arms and is shown by the dashed red curve in the figure. A secondary arm is defined as active when it is longer than the next active secondary arm closer to the primary tip. Two liquid phases are introduced in the framework because, in general, solute diffusion is governed by length scales of different orders of magnitude: the secondary arm spacing in the inter-dendritic liquid and the distance between the primary dendrite arms in the extra-dendritic liquid. The framework makes the following assumptions: at the microscopic level, the different phases are at thermal and mechanical equilibrium (i.e., have the same temperature and pressure); the inter-dendritic liquid is well-mixed (i.e., has a uniform concentration) and is at the equilibrium concentration (given by the phase diagram). The extra-dendritic liquid is, in general, undercooled. Note that the dendritic envelope (shown by the dashed red curve in Fig. 1) shall not be confused with the columnar front (shown by the thick dashed vertical line), as the liquid behind the columnar front is generally undercooled while the liquid behind the envelope is not. To develop a macroscale model using the framework of Wang and Beckermann [14], the local equations (i.e., equations that are valid at the microscopic scale) for each phase are formally averaged over a volume that contains all the phases present in the system and is called the Representative Elementary Volume (REV). Wang and Beckermann used their framework to develope a model for equiaxed solidification in the presence of melt convection [15–17] and a model for the columnar to equiaxed transition in the absence of melt convection [18]. Martorano et al. [19] used the framework to develope another model for the columnar to equiaxed transition in the absence of melt convection.

Although models that incorporate melt convection and liquid undercooling have been already developed using the framework of Wang and Beckermann [14] and have been successfully used to simulate solidification in different systems [20–25], more research in this area is still needed for at least three reasons. First, most of the models that are available are three-phase models and the existence of the third phase makes their numerical implementation significantly more complex than the two-phase models which (as already discussed and due to their relative simplicity) have been extensively used in the literature to predict melt convection in the absence of liquid undercooling. This extra complexity increases the computational cost of the models and, more importantly, has created problems in several previous studies, especially in predicting sensitive phenomena such as channel segregates. For example, in the study of Carozzani et al. [7], where simulations of a solidification experiment were performed, channels (observed in the experiment) were not predicted and, although the reason for the failure to predict them was not entirely clear, it was believed to be due to the lack of computational resources and model uncertainties; as another example, in a previous study by the authors [26], where the same experiment was simulated, the model that accounted for liquid undercooling failed to predict channels. A two-phase model that is simpler to implement than the three-phase models but still incorporates both melt convection and liquid undercooling can help alleviate these problems (by allowing one to more readily predict melt convection and channel segregates in the presence of liquid undercooling). Second, there are still some open questions in this research area. For example, a macroscale model that accounts for liquid undercooling is obviously more general than one that does not and can, therefore, be expected to recover that model at some limiting values of its parameters. This recovery has, to the authors' best knowledge, never been investigated in the literature. Third, it should be noted that the interplay between liquid undercooling and melt convection during solidification and their effect on the final macrosegregation pattern or channel segregates have never been investigated in any detail. For example, it is known from the literature that channel segregates are sensitive to the mesh spacing [27] or the relation used to calculate the permeability of the mush [28]; therefore, it is reasonable to expect that they are also sensitive to the liquid undercooling. The extent of this sensitivity, however, has not been investigated.

The main objective of this paper is to develop a two-phase model that incorporates melt convection and liquid undercooling ahead of the columnar front. This model, which is referred to as a truncated-Scheil-type model (for reasons that will be discussed in Section 2.1), is derived from a three-phase columnar solidification model. The three-phase

model itself is developed using the framework of Wang and Beckermann [14] and is similar to their equiaxed solidification model [15–17]. In addition, a robust and easy-to-implement numerical scheme to update solid fractions during solidification is developed and, for the first time in the field of macroscale modeling of solidification, complex movements of the columnar front, due to the presence of strong melt convection, channel segregates and liquid undercooling, were tracked. Predictions of the truncated-Scheil-type and three-phase models, in the absence and presence of melt convection, and with different values of the dendrite tip selection parameter σ^*, are compared with the predictions of a Scheil-type model that neglects liquid undercooling entirely. The effects of liquid undercooling and melt convection on each other during solidification, on the final macrosegregation pattern, and on the channel segregates is investigated.

This paper is organized as follows: Section 2 introduces the different models and outlines their governing equations. Section 3 discusses the numerical solution of the governing equations and a scheme that is developed to calculate solid fractions during solidification. Section 4 introduces the numerical solidification benchmark problem. Finally, Section 5 discusses predictions of the different models and with the different values of σ^*.

2. Three different models: the three-phase, truncated-Scheil-type, and Scheil-type

This study explores three models that differ mainly in the assumption that they make with respect to liquid undercooling. Section 2.1 presents an overview of these models. Section 2.2 presents the derivation of the governing equations for the models, and the final sub-section summarizes the similarities and the differences between them.

2.1. Overview of the three models

The three-phase model is developed using the multiphase modeling framework of Wang and Beckermann [14] and is similar to the model that Wang and Beckermann [15–17] developed using that framework. The latter model is referred to as the WB model hereafter. In addition to the fundamental assumptions made in the framework of Wang and Beckermann [14] (see paragraph four of Section 1), the three-phase model developed here and the WB model both assume that the thermophysical properties of the different phases are equal and constant (except for the liquid density in the buoyancy term of the momentum equation); therefore, solidification shrinkage is disregarded.

Next, the main differences between the three-phase model developed here and the WB model are discussed. First, our model is for columnar solidification and, therefore, disregards solid motion, while the WB model was for equiaxed solidification, and incorporated that motion. Second, for reasons that will become clear subsequently, the model developed here requires tracking of the columnar front, while the WB model did not. Third, because the main objective of this study is to develop a two-phase model (see Section 1) with only one liquid phase, the three-phase model developed here assumes that the inter-dendritic and extra-dendritic liquids have the same velocity and that there is no solute diffusion in the solid, while the WB model did not make those assumptions.

The truncated-Scheil-type model is a two-phase model that is derived from the three-phase model by making an additional assumption to those of the three-phase model: the liquid behind the columnar front is not undercooled. It is shown that, because of this single assumption, the truncated-Scheil-type model becomes significantly less complex than the three-phase model, while the predictions of the two models are nearly identical. The reason that this two-phase model is referred to as the truncated-Scheil-type model is that, similar to the truncated-Scheil model of Flood and Hunt [13], it disregards solute diffusion in the solid and liquid undercooling behind the columnar front but takes into account liquid undercooling ahead of the columnar front. It is emphasized that, unlike the truncated-Scheil model of Flood and Hunt [13], the truncated-Scheil-type model developed here incorporates melt convection, and to make that distinction clear, it is referred to as the truncated-Scheil-type model (instead of just truncated-Scheil). Finally, the third model, similar to the one used in simulating the numerical solidification benchmark problem [11], disregards liquid undercooling entirely but unlike that model, which assumed infinite solute diffusion in the solid, assumes no solute diffusion in the solid. The third model is hereafter referred to as the Scheil-type model.

Before proceeding, it is useful to summarize the main assumptions behind the three-phase, truncated-Scheil-type, and Scheil-type models. These models all disregard solid motion and solute diffusion in the solid. The three-phase model assumes that the inter-dendritic and extra-dendritic liquids have the same velocity but makes no simplifying assumption with respect to liquid undercooling. The truncated-Scheil-type model disregards liquid undercooling behind the columnar front, while the Scheil-type model disregards it both behind and ahead of the columnar front. The governing equations for these models are introduced next.

2.2. Governing equations

In this sub-section, first the equations that the three models share are listed. Then, the equations for the solute conservation in the liquid(s) in the different models are outlined. After that, the thermodynamic and constitutive relations of the models are listed.

2.2.1. Overarching equations: conservation of mass, momentum, energy, and solute in solid

The continuity equation reads [15]

$$\nabla \cdot \left(g_l \bar{\boldsymbol{v}}_l\right) = \nabla \cdot \boldsymbol{v} = 0 \tag{1}$$

where g_l, $\bar{\boldsymbol{v}}_l$, and $\boldsymbol{v}$ are the liquid fraction (in the three-phase model, the liquid fraction is equal to the inter-dendritic liquid fraction plus the extra-dendritic liquid fraction), average liquid velocity, and superficial liquid velocity, respectively. Note that the first equality follows from the definition of the superficial liquid velocity and, in the three-phase model, the assumption that the inter-dendritic and extra-dendritic liquidus have the same velocity. The second equality follows from the assumption that the solid is motionless and the density of the liquid is constant.

The liquid momentum equation in terms of the average liquid velocity $\bar{\boldsymbol{v}}_l$ reads [15]

$$\rho_0 \frac{\partial}{\partial t}\left(g_l \bar{\boldsymbol{v}}_l\right) + \rho_0 \nabla \cdot \left(g_l \bar{\boldsymbol{v}}_l \bar{\boldsymbol{v}}_l\right) = -g_l \nabla \bar{p} + \nabla \cdot \left[\mu_l \nabla \left(g_l \bar{\boldsymbol{v}}_l\right)\right] + g_l \tilde{\rho}_l \boldsymbol{g} - \frac{\mu_l g_l^2}{K} \bar{\boldsymbol{v}}_l \tag{2}$$

where ρ_0, $\bar{p}$, μ_l, $\tilde{\rho}_l$, and K are the reference density, average pressure, liquid dynamic viscosity, liquid density in the buoyancy term, and permeability of the semi-solid mush, respectively. The liquid density in the buoyancy term is calculated from $\tilde{\rho}_l = \rho_0[1 - \beta_T(T - T_{ref}) - \beta_C(\bar{C}_l - C_{ref})]$, where β_T and β_C are the thermal and solutal expansion coefficients, respectively, and T_{ref} and C_{ref} are a reference temperature and solute concentration, respectively. The permeability of the semi-solid mush is calculated from the Kozeny–Carman relation: $K = \lambda_2^2 {g_l}^3/[180(1 - g_l)^2]$ [11], where λ_2 is the secondary dendrite arm spacing.

It is common to re-write Eq. (2) in terms of the superficial liquid velocity $\boldsymbol{v}$. The first term on the left-hand side and the second and fourth terms on the right-hand side can be written in terms of $\boldsymbol{v}$ using $\boldsymbol{v} = g_l \bar{\boldsymbol{v}}_l$ (see Eq. (1)). To re-write the second term in terms of $\boldsymbol{v}$, one needs to first recognize that $\nabla \cdot (g_l \bar{\boldsymbol{v}}_l \bar{\boldsymbol{v}}_l) = \nabla \cdot (\bar{\boldsymbol{v}}_l \boldsymbol{v}) = (\bar{\boldsymbol{v}}_l \cdot \nabla)(\boldsymbol{v}) + \bar{\boldsymbol{v}}_l(\nabla \cdot \boldsymbol{v}) = (1/g_l)(\boldsymbol{v} \cdot \nabla)\boldsymbol{v}$, where the right-hand side of the third equality can be re-written as $(\boldsymbol{v} \cdot \nabla)\boldsymbol{v} = \nabla \cdot (\boldsymbol{v}\boldsymbol{v}) - \boldsymbol{v}(\nabla \cdot \boldsymbol{v}) = \nabla \cdot (\boldsymbol{v}\boldsymbol{v})$. Note that, in these relations, the equalities $\nabla \cdot (\bar{\boldsymbol{v}}_l \boldsymbol{v}) = (\bar{\boldsymbol{v}}_l \cdot \nabla)(\boldsymbol{v}) + \bar{\boldsymbol{v}}_l(\nabla \cdot \boldsymbol{v})$ and $(\boldsymbol{v} \cdot \nabla)\boldsymbol{v} = \nabla \cdot (\boldsymbol{v}\boldsymbol{v}) - \boldsymbol{v}(\nabla \cdot \boldsymbol{v})$ hold for any pair of vectors $\bar{\boldsymbol{v}}_l$ and $\boldsymbol{v}$. Also, the last

equalities in these relations follow simply from Eq. (1). Combining these two relations, one gets $\nabla\cdot(g_l\bar{\boldsymbol{v}}_l\bar{\boldsymbol{v}}_l)=(1/g_l)\nabla\cdot(\boldsymbol{v}\boldsymbol{v})$ and substituting this into Eq. (2) gives the final momentum equation in terms of the superficial liquid velocity $\boldsymbol{v}$

$$\rho_0\frac{\partial\boldsymbol{v}}{\partial t}+\rho_0\frac{1}{g_l}\nabla\cdot(\boldsymbol{v}\boldsymbol{v})=-g_l\nabla\bar{p}+\nabla\cdot\left(\mu_l\nabla\boldsymbol{v}\right)+g_l\tilde{\rho}_l\boldsymbol{g}-\frac{\mu_l g_l}{K}\boldsymbol{v} \tag{3}$$

The energy equation reads [15]

$$\frac{\partial T}{\partial t}+\nabla\cdot(\boldsymbol{v}T)=\alpha_0\nabla^2T+\frac{h_{sl}}{c_p}\frac{\partial g_s}{\partial t} \tag{4}$$

where T, $\alpha_0=k_0/(\rho_0c_p)$, h_{sl}, c_p, and $g_s=1-g_l$ are the temperature, thermal diffusivity, latent heat, specific heat capacity, and solid fraction, respectively.

The equation for the solute conservation in the solid reads [15]

$$\frac{\partial}{\partial t}\left(g_s\bar{C}_s\right)=k_0C_l^*\frac{\partial g_s}{\partial t} \tag{5}$$

where $\bar{C}_s$, k_0, and C_l^* are the average solute concentration in the solid, solute partition coefficient, and equilibrium solute concentration, respectively.

2.3. Solute conservation in liquid(s)

Recall from Section 2.1 that the three-phase model has two liquid phases: the inter-dendritic and extra-dendritic liquids. In this section, the equations for solute conservation in the two liquids are listed first, and then these equations are used to derive the equation for the liquid solute conservation in the truncated-Scheil-type and Scheil-type models.

2.3.1. Three-phase model

The equation for solute conservation in the inter-dendritic liquid reads [14–17]

$$\rho_0\frac{\partial}{\partial t}\left(g_d\bar{C}_d\right)+\rho_0\nabla\cdot\left(g_d\bar{\boldsymbol{v}}_l\bar{C}_d\right)=-k_0\Gamma_{sd}\bar{C}_d-\Gamma_{ed}\bar{C}_d-\rho_0\frac{S_{env}D_0}{\delta_{env}}\left(\bar{C}_d-\bar{C}_e\right) \tag{6}$$

where g_d, $\bar{C}_d$, Γ_{sd}, Γ_{ed}, S_{env}, δ_{env}, and $\bar{C}_e$ are the inter-dendritic liquid fraction, average solute concentration in the inter-dendritic liquid, average interfacial mass generation source due to phase-change at the interface between the solid and inter-dendritic liquid and at the interface between the inter-dendritic liquid and extra-dendritic liquid, surface area of the envelope per unit volume of the REV, average diffusion length around the envelope, and average solute concentration in the extra-dendritic liquid, respectively.

The equation for the solute conservation in the extra-dendritic liquid reads [14–17]

$$\rho_0\frac{\partial}{\partial t}\left(g_e\bar{C}_e\right)+\rho_0\nabla\cdot\left(g_e\bar{\boldsymbol{v}}_l\bar{C}_e\right)=\Gamma_{ed}\bar{C}_d+\rho_0\frac{S_{env}D_0}{\delta_{env}}\left(\bar{C}_d-\bar{C}_e\right) \tag{7}$$

where $g_e=1-g_s-g_d$ is the extra-dendritic liquid fraction.

Before proceeding, it is useful to discuss the physical meaning of the different terms on the right-hand sides of Eqs. (6) and (7). On the right-hand side of Eq. (6), the first term represents the solute transfer from the inter-dendritic liquid to the solid at the interface between these two phases due to movement of that interface (i.e., due to solidification); the second and third terms represent the solute transfer from the inter-dendritic liquid to the extra-dendritic liquid at the interface between these phases, due to the movements of that interface and due to the diffusion at that interface, respectively. Note that the negative sign of all the terms on the right-hand side stems from the fact that, at the microscopic level, solute transfer is always from the inter-dendritic liquid to the neighboring phases (because the solute concentration in the inter-dendritic liquid is higher than the solute concentration in the neighboring phases). In Eq. (7), the terms on the right-hand side are the counterparts of the last two terms on the right-hand side of Eq. (6), on the extra-dendritic liquid side of the interface between the two liquids.

Next, on the right-hand side of Eqs. (6) and (7), the interfacial mass generation sources due to phase-change (i.e., Γ_{sd} and Γ_{ed}) and the convective fluxes on the left-hand side (i.e., $\nabla\cdot(g_d\bar{\boldsymbol{v}}_l)$ and $\nabla\cdot(g_e\bar{\boldsymbol{v}}_l)$) are rewritten in terms of the phase fractions and superficial liquid velocity $\boldsymbol{v}=g_l\bar{\boldsymbol{v}}_l$, respectively. To substitute Γ_{sd} and Γ_{ed}, one first needs to write the mass conservation equations for the solid and extra-dendritic liquids as follows [14–17]

$$\rho_0\frac{\partial g_s}{\partial t}=\Gamma_{sd} \tag{8}$$

$$\rho_0\frac{\partial g_e}{\partial t}+\rho_0\nabla\cdot\left(g_e\bar{\boldsymbol{v}}_l\right)=\Gamma_{ed}=-\rho_0S_{env}w_{env} \tag{9}$$

where w_{env} is the average growth velocity of the envelope.

Before proceeding, it is insightful to understand the physical meaning of Eqs. (8) and (9). Eq. (8) states that, in the absence of solid motion, the rate of increase in the solid mass per unit volume of the REV (i.e., the left-hand side of the equation) is equal to the mass exchange rate at the interface between the solid and inter-dendritic liquid due to the movements of this interface (i.e., the left-hand side of the equation).

In Eq. (9), the first equality states that the rate of increase in the extra-dendritic liquid mass per unit volume of the REV (i.e., the term $\rho_0\partial g_e/\partial t$) plus the rate at which the extra-dendritic liquid leaves the REV due to the flow of this liquid (i.e., the term $\rho_0\nabla\cdot(g_e\bar{\boldsymbol{v}}_l)$), is equal to the mass exchange rate at the interface between the two liquids due to the movements of this interface (i.e., Γ_{ed}). The second equality in Eq. (9) is obtained by modeling the interfacial mass exchange rate as the product of surface area of the interface (i.e., the envelope) per unit volume of the REV and the mean interfacial flux [14]. The second term on the left-hand side of the first equality in Eq. (9) shall not be confused with a similar term that would have appeared on the right-hand side of Eq. (8), if grain movement had been taken into account (see, for example, the solid momentum equation in Table II of [15]). Further examining Eq. (9) reveals another interesting point: due to the presence of the flow term in this equation (i.e., the term $\rho_0\nabla\cdot(g_e\bar{\boldsymbol{v}}_l)$), the extra-dendritic liquid fraction can change even when the envelope is not growing (i.e., when $w_{env}=0$).

Substituting Γ_{ed} from the first equality in Eq. (9) into Eq. (7) and noting that in Eq. (7), the second term on the left hand side can be re-written using $\nabla\cdot(g_e\bar{\boldsymbol{v}}_l\bar{C}_e)=\nabla\cdot[\boldsymbol{v}(g_e/g_l)\bar{C}_e]=(g_e/g_l)\nabla\cdot(\boldsymbol{v}\bar{C}_e)+\bar{C}_e\nabla\cdot(\boldsymbol{v}g_e/g_l)$ (where the first equality follows directly from the discussion below Eq. (1) and the second equality follows from the mathematical identity governing the divergence of a product of a scalar and a vector and the fact that $\boldsymbol{v}\cdot\nabla(g_e/g_l)=\nabla\cdot(\boldsymbol{v}g_e/g_l)$ due to Eq. (1)), Eq. (7) becomes

$$\begin{aligned}&g_e\frac{\partial\bar{C}_e}{\partial t}+\frac{g_e}{g_l}\nabla\cdot\left(\boldsymbol{v}\bar{C}_e\right)\\&\quad=\left(\bar{C}_d-\bar{C}_e\right)\frac{\partial g_e}{\partial t}+\left(\bar{C}_d-\bar{C}_e\right)\nabla\cdot\left(\boldsymbol{v}\frac{g_e}{g_l}\right)+\frac{S_{env}D_0}{\delta_{env}}\left(\bar{C}_d-\bar{C}_e\right)\end{aligned} \tag{10}$$

Similarly, on the left-hand side of Eq. (6), Γ_{sd} and Γ_{ed} can be substituted using Eqs. (8) and (9), respectively, and the last term can be substituted from Eq. (10) to get

$$\begin{aligned}\frac{\partial}{\partial t}\left(g_d\bar{C}_d\right)+\nabla\cdot\left(g_d\bar{\boldsymbol{v}}_l\bar{C}_d\right)&=\left(1-k_0\right)\frac{\partial g_s}{\partial t}\bar{C}_d+\left[\frac{\partial g_d}{\partial t}+\nabla\cdot\left(g_d\bar{\boldsymbol{v}}_l\right)\right]\bar{C}_d\\&\quad-\left[g_e\frac{\partial\bar{C}_e}{\partial t}+\frac{g_e}{g_l}\nabla\cdot\left(\boldsymbol{v}\bar{C}_e\right)-\left(\bar{C}_d-\bar{C}_e\right)\frac{\partial g_e}{\partial t}-\left(\bar{C}_d-\bar{C}_e\right)\nabla\cdot\left(\boldsymbol{v}\frac{g_e}{g_l}\right)\right]\end{aligned} \tag{11}$$

Next, if the time and spatial derivatives on the left-hand-side are expanded, then the terms inside the first brackets on the right-hand-side can be dropped by their counterparts on the left-hand side and the result will be

$$g_d\frac{\partial \bar{C}_d}{\partial t}+g_d\bar{\boldsymbol{v}}_l\cdot\nabla\bar{C}_d=\left(1-k_0\right)\frac{\partial g_s}{\partial t}\bar{C}_d -\left[g_e\frac{\partial \bar{C}_e}{\partial t}+\frac{g_e}{g_l}\nabla\cdot\left(\boldsymbol{v}\bar{C}_e\right)-\left(\bar{C}_d-\bar{C}_e\right)\frac{\partial g_e}{\partial t}-\left(\bar{C}_d-\bar{C}_e\right)\nabla\cdot\left(\boldsymbol{v}\frac{g_e}{g_l}\right)\right] \quad (12)$$

Next, Eq. (12) needs to be re-written in the conservative form and in terms of the superficial liquid velocity $\boldsymbol{v}$ only. Using identities $(\bar{C}_d-\bar{C}_e)\nabla\cdot(\boldsymbol{v}g_e/g_l)=\nabla\cdot[\boldsymbol{v}(g_e/g_l)(\bar{C}_d-\bar{C}_e)]-\boldsymbol{v}(g_e/g_l)\cdot\nabla(\bar{C}_d-\bar{C}_e)$ and $g_d\bar{\boldsymbol{v}}_l\cdot\nabla\bar{C}_d=(g_l-g_e)(\boldsymbol{v}/g_l)\cdot\nabla\bar{C}_d=\nabla\cdot(\boldsymbol{v}\bar{C}_d)-(g_e/g_l)\nabla\cdot(\boldsymbol{v}\bar{C}_d)$, Eq. (12) becomes

$$g_l\frac{\partial \bar{C}_d}{\partial t}+\nabla\cdot\left(\boldsymbol{v}\bar{C}_d\right)=\left(1-k_0\right)\bar{C}_d\frac{\partial g_s}{\partial t} -\frac{\partial}{\partial t}\left[g_e\left(\bar{C}_e-\bar{C}_d\right)\right]-\nabla\cdot\left[\boldsymbol{v}\frac{g_e}{g_l}\left(\bar{C}_e-\bar{C}_d\right)\right] \quad (13)$$

which is the final form of the equation for solute balance in the inter-dendritic liquid.

2.3.2. Truncated-Scheil-type and Scheil-type models

To derive the equation for the solute conservation in the liquid for the truncated-Scheil-type and Scheil-type models, the average solute concentration in the liquid $\bar{C}_l$ is defined as

$$g_l\bar{C}_l=g_d\bar{C}_d+g_e\bar{C}_e \quad (14)$$

The equation for solute conservation in the liquid is obtained by adding up Eqs. (6) and (7), substituting $g_d\bar{C}_d+g_e\bar{C}_e$ from Eq. (14), $g_l\bar{\boldsymbol{v}}_l$ from the first equality in Eq. (1), Γ_{sd} from Eq. (8), and $\bar{C}_d\partial g_s/\partial t=C_l^*\partial g_s/\partial t$ as

$$\frac{\partial}{\partial t}\left(g_l\bar{C}_l\right)+\nabla\cdot\left(\boldsymbol{v}\bar{C}_l\right)=-k_0C_l^*\frac{\partial g_s}{\partial t} \quad (15)$$

Expanding the time derivative on the left-hand side and adding and subtracting $k_0\bar{C}_l\partial g_l/\partial t$ to and from the right-hand side gives

$$g_l\frac{\partial \bar{C}_l}{\partial t}+\nabla\cdot\left(\boldsymbol{v}\bar{C}_l\right)=k_0\left(C_l^*-\bar{C}_l\right)\frac{\partial g_l}{\partial t}+\bar{C}_l\left(1-k_0\right)\frac{\partial g_s}{\partial t} \quad (16)$$

Next, Eq. (16) is analyzed. Note that in deriving this equation, no additional assumptions have been made. In other words, this equation is as general as Eqs. (10) and (13) of the three-phase model. In fact, in that model, one can replace Eq. (10) or (13) with Eq. (16), without loss of generality. The second term on the right-hand side of Eq. (16) represents solute rejection (assuming $k_0<1$) during solidification. Understanding the first term on the right-hand side is key in simplifying the three-phase model and developing the truncated-Scheil-type and Scheil-type models. This term consists of $\partial g_l/\partial t$, which represents solidification rate, and $C_l^*-\bar{C}_l$, which is linked to the liquid undercooling. If one disregards liquid undercooling entirely (i.e., assumes that $C_l^*-\bar{C}_l$ is zero everywhere), then, the first term on the right-hand side can be dropped, and Eq. (16) will reduce to the equation for the liquid solute balance in the Scheil-type model. The key point to realize here is that this term will still be zero even if one assumes that liquid can be undercooled in the absence of local solidification (i.e., $\partial g_l/\partial t=0$), but it is not undercooled in the presence of local solidification (i.e., $C_l^*=\bar{C}_l$ when $\partial g_l/\partial t\neq 0$). For fully columnar solidification, this is equivalent to stating that the liquid behind the columnar front is assumed not to be undercooled, while the liquid ahead of the columnar front is undercooled. Dropping this term gives the final form of the liquid solute balance equation for the truncated-Scheil-type and Scheil-type models as

$$g_l\frac{\partial \bar{C}_l}{\partial t}+\nabla\cdot\left(\boldsymbol{v}\bar{C}_l\right)=\bar{C}_l\left(1-k_0\right)\frac{\partial g_s}{\partial t} \quad (17)$$

2.4. Thermodynamic relations

Under the assumption of local thermodynamic equilibrium, the temperature at the interface between the solid and (inter-dendritic) liquid is given by the liquidus line of the phase diagram. In this section, the thermodynamic relations for the three-phase model are listed first, followed by a discussion of the slight, but important, modification to the relations of the three-phase model that is required to obtain the corresponding relations for the truncated-Scheil-type and Scheil-type models. To write down the thermodynamic relations, one first needs to recognize that these relations take different forms during primary and eutectic solidification, and this is discussed next.

Primary columnar solidification takes place for temperatures below the local liquidus temperature and, obviously, only in the region behind the columnar front. In the three-phase model, these regions are distinguished (from regions ahead of the columnar front) by positive values of the phase-field ϕ. The phase-field ϕ is itself calculated from an interface tracking method that will be further explored in Section 2.6. During primary solidification, the inter-dendritic liquid solute concentration is equal to the equilibrium solute concentration C_l^*, which is given by the liquidus line of the phase diagram.

Eutectic solidification starts when $\bar{C}_d$ reaches the eutectic concentration C_{eut}, while g_l is still non-zero. During eutectic solidification, the temperature is equal to the eutectic temperature T_{eut}, and there is no solute rejection due to solidification. Therefore, the partition coefficient needs to be set to unity. These premises can be stated mathematically as

$$\begin{aligned}&\text{Primary solidification: } T\le T_{liq}\left(\bar{C}_d\right)\text{ and }\phi>0 \quad\rightarrow\quad \bar{C}_d=C_l^*=\frac{T-T_f}{m_l}\\ &\text{Eutectic solidification: } \bar{C}_d=C_{eut}\text{ and }g_l\ge 0 \quad\rightarrow\quad T=T_{eut}\quad\text{and}\quad k_0=1\end{aligned} \quad (18)$$

where $T_{liq}(\bar{C}_d)=T_f+m_l\bar{C}_d$ is the liquidus temperature corresponding to the local inter-dendritic liquid concentration $\bar{C}_d$. Again, in Eq. (18), $\phi>0$ represents regions behind the columnar front. For an equiaxed solidification model, such as the one developed by Wang and Beckermann [15], the left-hand side of the first arrow needs to be replaced by a condition representing temperatures below the nucleation temperature. Therefore, such a model will not require interface tracking and this is one of the important differences between the three-phase columnar solidification model developed here and the three-phase equiaxed solidification model of Wang and Beckermann [15].

The thermodynamic relations for the truncated-Scheil-type and Scheil-type models are similar to Eq. (18). The only difference, which is of critical importance, is that for the truncated-Scheil-type model, $\bar{C}_d$ in this equation must be replaced with $\bar{C}_l$; for the Scheil-type model, in addition to replacing $\bar{C}_d$ with $\bar{C}_l$, the condition $\phi>0$ needs to be removed. Therefore, this model does not require calculation of ϕ (i.e., interface tracking).

2.5. Constitutive relations for the envelope surface area and diffusion length in the three-phase model

In the three-phase model, the final forms of the equations for the solute balance in the liquids (i.e., Eqs. (10) and (13)) contain the envelope surface area per unit volume of the REV, S_{env}, and the average diffusion length around the envelope δ_{env}. These two quantities need to be calculated using additional constitutive relations. The envelope surface area S_{env} is calculated from [19]

$$S_{env}=\begin{cases}0 & \phi<0\\ \frac{3(1-g_e)^{2/3}}{R_f} & \phi\ge 0\end{cases} \quad (19)$$

where $R_f=\lambda_1/2$ is the final envelope radius and λ_1 is the primary arm spacing. The first part of the relation simply reflects the fact that in columnar solidification, the envelope surface area ahead of the columnar front is, obviously, zero.

The diffusion length δ_{env} is calculated from the relation proposed by Martorano et al. [19], which reads

$$\frac{\delta_{env}}{R_e} = \frac{3R_e e^{Pe}}{R_f^3 - R_e^3}\int_{R_e}^{R_f}\left(\int_{R_e}^{r}\frac{e^{-Pe\frac{r'}{R_e}}}{r'^2}dr'\right)r^2 dr \tag{20}$$

where $Pe = w_{env}R_e/D_l$ is the growth Péclet number and $R_e = R_f(1-g_e)^{1/3}$ is the instantaneous envelope radius.

Note that Eqs. (19) and (20) were derived for equiaxed spherical envelopes. Because the envelope of a columnar dendrite is not spherical, one might wonder why those equations are used in our three-phase model, which is, again, for columnar solidification. The reason is that, as shown in Section 5, for columnar solidification, liquid undercooling behind the columnar front can be disregarded. Therefore, Eqs. (19) and (20) are not an important part of the model, and using them, instead of more realistic relations that are available in the literature [29], should not distract. In any case, the difference can be expected to be small.

2.6. Columnar front tracking for the three-phase and truncated-Scheil-type models

The three-phase and truncated-Scheil-type models, as opposed to the Scheil-type model (see the discussion in the last paragraph of Section 2.4), contain the phase field variable ϕ (see Eqs. (18) and (19)), which needs to be calculated using an interface tracking method. Before discussing the method that was used in this study to track the columnar front, it is useful to review the previous studies where the columnar front was tracked. In studies of Martorano et al. [19], Wang and Beckermann [18], and Browne and co-authors [30–38] the columnar front was tracked in the absence of melt convection. In other studies by Browne and co-authors [39,40], the columnar front was tracked in the presence of melt convection but the solutal buoyancy forces were disregarded, and melt convection was due to the thermal buoyancy forces only. Seredynski and Banaszek [41] and Banaszek and Seredynski [42] tracked the columnar front in the presence of melt convection without disregarding the solutal buoyancy forces, but their studies provide no discussion on the channel segregates and, in fact, it is not even clear if channels were predicted or not. In the present study, the columnar front is tracked in the presence of strong melt convection, driven by both thermal and solutal buoyancy forces and channel segregates.

In the present study, the method used to calculate ϕ (i.e., to track the columnar front) is the phase-field sharp interface tracking method of Sun and Beckermann [43]. The columnar front is represented by the isocontour $\phi = 0$; regions behind and ahead of the columnar front are represented by $\phi > 0$ and $\phi < 0$, respectively. Initially (i.e., at $t = 0$), ϕ is equal to minus unity everywhere in the simulation domain except at the boundary from which the columnar grains grow, where ϕ is set to zero; in other words, the columnar front is assumed to be initially located at the domain boundary from which solidification starts. For $t > 0$, ϕ is calculated from [43]

$$\frac{\partial\phi}{\partial t} + \boldsymbol{w}_{env}\cdot\nabla\phi = b\left[\nabla^2\phi + \frac{\phi(1-\phi^2)}{W^2} - |\nabla\phi|\nabla\cdot\left(\frac{\nabla\phi}{|\nabla\phi|}\right)\right] \tag{21}$$

where $\boldsymbol{w}_{env}$ is the envelope average growth velocity vector and b and W are numerical parameters that control the stability of the method and the finite thickness of the columnar front region on the numerical mesh, respectively, and are calculated using the relations in Sun and Beckermann [43]. To calculate $\boldsymbol{w}_{env}$, it is first assumed that the envelope grows in the direction of the local thermal gradient (i.e., perpendicular to the local isotherms):

$$\boldsymbol{w}_{env} = w_{env}\frac{\nabla T}{|\nabla T|} \tag{22}$$

where w_{env} is the magnitude of the average growth velocity vector which, in the three-phase model, is calculated from [19]

$$w_{env} = \frac{4\sigma^* D_0 m_l(k_0-1)C_l^*}{\Gamma}\left[Iv^{-1}(\Omega_e)\right]^2 \tag{23}$$

where σ^*, Γ, $Iv^{-1}()$, and Ω_e are the tip selection parameter, Gibbs–Thomson coefficient, inverse Ivantsov function and average undercooling in the extra-dendritic liquid, which is defined as [19]

$$\Omega_e = \frac{C_l^* - \bar{C}_e}{C_l^*(1-k_0)} \tag{24}$$

In Eq. (23), the inverse Ivantsov function is calculated from [19]

$$Iv^{-1}(\Omega_e) = 0.4567\left(\frac{\Omega_e}{1-\Omega_e}\right)^{1.195} \tag{25}$$

In the truncated-Scheil-type model, w_{env} is calculated from Eqs. (23) to (25), however, Ω_e in these equations needs to be replaced with the average undercooling in the liquid Ω_l, which is defined as

$$\Omega_l = \frac{C_l^* - \bar{C}_l}{C_l^*(1-k_0)} \tag{26}$$

As already discussed in Section 2.1, the truncated-Scheil-type-model does not account for liquid undercooling behind the columnar front; therefore, Ω_l predicted by this model (from Eq. (26)) is expected to be zero for $\phi > 0$. It is now interesting to discuss how this expected value for Ω_l is obtained from the governing equations. According to the thermodynamic relation (see Eq. (18) and the discussion below), for $\phi > 0$, one has $C_l^* = \bar{C}_l$, which, from Eq. (26), results in $\Omega_l = 0$, as expected. In the three-phase model, the liquid undercooling behind the columnar front (predicted from Eq. (24)) can be, in general, non-zero because, in that model, for $\phi > 0$, one has $C_l^* = \bar{C}_d$ as opposed to $C_l^* = \bar{C}_e$; therefore, Eq. (24) can predict non-zero values for Ω_l even when $\phi > 0$.

For the Scheil-type model, an "undercooling" can be calculated from Eq. (26), but the values of Ω_l will be either zero (inside the mush) or negative (in the superheated liquid). The reason is, as discussed below Eq. (18), in the Scheil-type model, during solidification (i.e., when $T \le T_{liq}(\bar{C}_l)$), one has $C_l^* = \bar{C}_l$ and therefore (from Eq. (26)) $\Omega_l = 0$; in the absence of solidification (i.e., when $T > T_{liq}(\bar{C}_l) = T_f + m_l\bar{C}_l$) one has $C_l^* < \bar{C}_l$ (note that $m_l < 0$) and therefore $\Omega_l < 0$.

2.7. Convergence of the three-phase and truncated-Scheil-type models to the Scheil-type model

Recall from the discussion in Section 2 that at some limiting values of the model parameters, the three-phase and truncated-Scheil-type models, which account for liquid undercooling, are expected to converge to the Scheil-type model, which does not account for liquid undercooling. Now that the equations for these models have been listed, this convergence can be discussed in more detail by examining Eq. (23) and the role of σ^* in that equation and, therefore, in the truncated-Scheil-type and three-phase models. In Eq. (23), if one increases σ^* to an effectively infinite value, Ω_e needs to become infinitely small, but still non-zero, so that both sides of the equation remain finite (note that, regardless of the value of σ^*, w_{env} needs to have a finite value that is less than the liquidus velocity). An infinitely small value for the liquid undercooling means that the Scheil-type model is recovered. In other words, it is reasonable to conjecture that by increasing σ^* in the truncated-Scheil-type and three phase models, these models converge to the Scheil-type model. The accuracy of this statement will be examined in the Results section.

It is also interesting to discuss how the above discussion on the role of σ^* is connected to the formal definition of σ^* in theories of dendritic growth [44]. In those theories, σ^* is defined as a constant that is inversely proportional to $V_t R_t^2$, where $V_t (= w_{env})$ and R_t are the tip velocity and radius, respectively. Therefore, increasing σ^* simply means that the product $V_t R_t^2$ needs to decrease. Now, consider quasi-steady growth of a columnar front during directional solidification, where the velocity of the columnar front is equal to the velocity of the isotherm that coincides with the front. Because in directional solidification the value of σ^* has no significant influence on the temperature distribution, increasing σ^* will not change the isotherm velocities nor V_t; therefore, to have $V_t R_t^2$

decrease, R_t will have to decrease. A decrease in R_t while V_t is constant indicates that the tip Peclet number $Pe_t = V_t R_t/2D_0$ will decrease, and that, from the Ivantsov relation, indicates that the liquid undercooling needs to decrease. Therefore, increasing σ^* to an effectively infinite value will decrease the liquid undercooling to an infinitely small value, and that is consistent with the above discussion on the role of σ^*.

2.8. Summary of the equations of the models

Before proceeding it is useful to summarize the equations for each of the models. The equations for conservation of mass, momentum, energy, and solute in the solid in all of these models are Eqs. (1), (3), (4), and (5), respectively. The three phase model has three additional conservation equations: (9), (10), and (13) for conservation of mass and solute in the extra-dendritic and inter-dendritic liquids, respectively. The truncated-Scheil-type and Scheil-type models have only one additional conservation equation: (17) for the conservation of solute in liquid. The rest of the equations of the three-phase model are Eqs. (18)–(25). The remaining equations of the truncated-Scheil-type model are the modified version of Eq. (18) and Eqs. (21)–(23) and (25) and (26). The remaining equation for the Scheil-type model is the modified version of Eq. (18).

3. Numerical solution of the governing equations

In this section, the numerical solution of the strongly coupled and highly nonlinear model equations is discussed. In the first sub-section, a numerical scheme that was developed to update the solid fraction during solidification is outlined. In the sub-section after that, details about the numerical solution of the equations are discussed.

3.1. Solid fraction updating scheme

Note that the models introduced in the previous section do not have an explicit relation for the solid fraction g_s. Numerical implementations of these models, however, require a relation that can be used to calculate g_s. In other words, a scheme to update the solid fraction is required. Such a scheme is developed in this section.

To develop a scheme to update the solid fraction, one first needs to acknowledge that, in Eq. (18), the equalities on the right-hand side of the arrows will be satisfied only if the "correct" solid fraction is used in calculating the temperature and (inter-dendritic) liquid solute concentration. An imbalance between the two sides of these equalities indicates that the solid fraction is inaccurate and needs to be corrected by an amount that can be assumed to be proportional to that imbalance. For the three-phase model, the relation to correct the solid fraction can be written as

$$\begin{aligned} &\text{Primary solidification}: \quad g_s^{n+1} = g_s^n + \frac{\partial g_s}{\partial T} m_l \left(C_l^* - \bar{C}_d\right) \\ &\text{Eutectic solidification}: \quad g_s^{n+1} = g_s^n + \frac{\partial g_s}{\partial T} \left(T_{eut} - T\right) \end{aligned} \tag{27}$$

where the superscripts $n+1$ and n refer to the current and previous iteration levels, respectively. Note that, at each time step, updating the solid fraction using Eq. (27) should be continued until $g_s^{n+1} = g_s^n$ (within the numerical precision); this will guarantee that at the end of the iterations, or in other words after convergence, $C_l^* = \bar{C}_d$ during primary solidification and $T_{eut} = T$ during eutectic solidification, which will, in turn, indicate that the equalities on the right-hand side of Eq. (18) are satisfied. For the truncated-Scheil-type and Scheil-type models, $\bar{C}_d$ in the first equality of Eq. (27) needs to be replaced with $\bar{C}_l$. To complete the solid fraction updating scheme, the relations to calculate $\partial g_s/\partial T$ during primary and eutectic solidification need to be derived. Because the final relations for $\partial g_s/\partial T$ are the same in the three models, the rest of the derivation is shown only for the Scheil-type model.

To obtain a relation to calculate $\partial g_s/\partial T$ during the primary solidification, Eq. (17) is first discretized explicitly as

$$\left(1-g_s^{old}\right)\frac{\bar{C}_l - \bar{C}_l^{old}}{\Delta t} + \nabla\cdot\left(\vec{v}_m^{old}\bar{C}_l^{old}\right) = \left(1-k_0\right)\bar{C}_l\frac{g_s^n - g_s^{old}}{\Delta t} \tag{28}$$

The solute concentration in liquid can be substituted from the thermodynamic relation for the Scheil-type model (see Eq. (18) and the discussion below) to give

$$\begin{aligned} &\left(1-g_s^{old}\right)\frac{\left(T-T_f\right)/m_l - \bar{C}_l^{old}}{\Delta t} + \nabla\cdot\left(\boldsymbol{v}^{old}\bar{C}_l^{old}\right) \\ &= \frac{\left(1-k_0\right)\left(T-T_f\right)}{m_l}\frac{g_s^n - g_s^{old}}{\Delta t} \end{aligned} \tag{29}$$

Both sides of this equation are differentiated with respect to T to give

$$\left(1-g_s^{old}\right) = \left(1-k_0\right)\left(g_s^n - g_s^{old}\right) + \left(1-k_0\right)\left(T-T_f\right)\frac{\partial g_s}{\partial T} \tag{30}$$

This equation is rearranged to give

$$\frac{\partial g_s}{\partial T} = \frac{1 - g_s^n + k_0\left(g_s^n - g_s^{old}\right)}{\left(1-k_0\right)\left(T-T_f\right)} \tag{31}$$

To obtain a relation to calculate $\partial g_s/\partial T$ during the eutectic solidification, Eq. (4) is first discretized explicitly as

$$\frac{T - T^{old}}{\Delta t} + \nabla\cdot\left(\boldsymbol{v}^{old}T^{old}\right) = \alpha\nabla^2 T^{old} + \frac{h_{sl}}{c_l}\frac{g_s - g_s^{old}}{\Delta t} \tag{32}$$

Differentiating both sides of this equation with respect to g_s gives

$$\frac{\partial g_s}{\partial T} = \frac{c_l}{h_{sl}} \tag{33}$$

Combining Eqs. (31) and (33) one gets:

$$\begin{aligned} &\text{Primary solidification}: \quad \frac{\partial g_s}{\partial T} = \frac{1 - g_s^n + k_0\left(g_s^n - g_s^{old}\right)}{\left(1-k_0\right)\left(T-T_f\right)} \\ &\text{Eutectic solidification}: \quad \frac{\partial g_s}{\partial T} = \frac{c_l}{h_{sl}} \end{aligned} \tag{34}$$

The above solid fraction updating scheme was found to be robust and efficient. It should be mentioned that a similar method was developed by Guo and Beckermann [27], but one of the advantages of the method developed here is that it does not require calculating intermediate values for the solute concentrations; therefore, its implementation is relatively straightforward. Another advantage of this method concerns parallel computing in the code we have used, and that issue will be discussed further next.

3.2. In-house OpenFOAM codes

To solve the governing equations numerically, two in-house parallel computing codes, one for the three-phase model and one for the truncated-Scheil-type and Scheil-type models, were developed on the OpenFOAM platform [45,46]. OpenFOAM is a widely used open-source CFD code, but its built-in capabilities in simulating alloy solidification remain very limited. Here, only the major aspects of the numerical implementation of the models in OpenFOAM are discussed; for more details, the reader is urged to consult the corresponding author. It is emphasized that one of the advantages of OpenFOAM is that it allows one to create customized applications that can be run on multiple cores, after decomposing the simulation domain, without a need to make any modifications in the coding of the application. One can benefit from that advantage only if the implemented numerical methods do not require parallel-specific programming, and this is one of the main advantages of the present solid fraction updating scheme. In fact, we first implemented the scheme of Guo and Beckermann [27], and noticed that performing parallel computations with the application that was using their method is not possible by just simply decomposing the simulation domain.

The equations outlined in Section 2 and the solid fraction updating scheme developed in Section 3.1 were implemented in the codes. The temporal and advection terms were discretized using the standard Euler and upwind methods, respectively. The discretized equations were solved iteratively at each time step until the residual for the discretized partial differential equations and the error for the solid fraction all became less than a convergence criterion determined by the user. Pressure coupling was handled using OpenFOAM's PIMPLE algorithm.

Another critical numerical point concerns tracking of the columnar front. Recall that, in theory, the columnar front is an imaginary surface with no thickness; therefore, in the numerical simulations, the columnar front region (i.e., the region with $-1 < \phi < 1$) should be kept as thin as possible (two to three mesh cells on the numerical grid). This can be achieved only if the value of ϕ at a cell continues to increase even after the columnar front passes that cell (i.e., when ϕ becomes zero locally). In other words, $\partial\phi/\partial t$ needs to be positive not only for $-1 < \phi < 0$, but also for $0 < \phi < 1$. By examining Eq. (21), it is easy to acknowledge that positive values of $\partial\phi/\partial t$ for $0 < \phi < 1$ will occur only if $\boldsymbol{w}_{env}$ in that equation, and therefore w_{env} in Eqs. (22) and (23), are positive for $0 < \phi < 1$. However, as already discussed in Section 2, the truncated-Scheil-type model disregards liquid undercooling behind the columnar front; therefore, in that model, for $\phi > 0$, w_{env} will be strictly zero. As a result of that, using w_{env} calculated directly from Eq. (23) to calculate $\boldsymbol{w}_{env}$ from Eq. (22), and then using that $\boldsymbol{w}_{env}$ in Eq. (21) to calculate ϕ will result in a continuous increase in the thickness of the columnar front region. This increase is not physical and should be avoided.

In order to avoid the problem with the increase in the thickness of the columnar front and keep the columnar front region relatively sharp, the PDE-based multidimensional extrapolation method of Aslam [47] was used. By implementing this method, at the end of each time step during the simulations, the following equation was solved repeatedly

$$\frac{\partial \bar{\boldsymbol{w}}_{env}}{\partial \tau} + H(\phi)\hat{\boldsymbol{n}} \cdot \nabla \bar{\boldsymbol{w}}_{env} = 0 \tag{35}$$

until $\partial \bar{\boldsymbol{w}}_{env}/\partial\tau$ became nearly zero. In this equation, τ is a pseudo-time, $\hat{\boldsymbol{n}} = \nabla\phi/|\nabla\phi|$ is the unit vector normal to the columnar front, and $H(\phi)$ is the sharp Heaviside function that is calculated from

$$H(\phi) = \begin{cases} 1 & \phi > 0 \\ 0 & \phi \le 0 \end{cases} \tag{36}$$

Note that, the zero value for the Heaviside function ahead of the columnar front ensures that Eq. (35) will not modify the values of $\bar{\boldsymbol{w}}_{env}$ in those regions.

Again, the discussion provided in Section 3.2 covers only the major aspects of the numerical implementation of the models in OpenFOAM and for more details (on, for example, how to avoid parallel-specific problems when implementing similar solidification models in OpenFOAM), the reader is urged to consult the corresponding author.

4. Problem statement

4.1. Numerical solidification benchmark problem

The problem studied in this paper is the solidification numerical benchmark problem introduced in Bellet et al. [11]. A schematic of the problem is shown in Fig. 2. The problem consists of solidification of a lead-18 wt. pct. tin alloy in a rectangular cavity. The cavity is insulated from the top and bottom. Initially, the melt is stationary, and its temperature is uniform and equal to the liquidus temperature at the initial concentration $C_{ref} = 18$ wt. pct. Solidification starts by cooling the cavity from the sides through an external cooling fluid with ambient temperature T_∞ and an overall heat transfer coefficient h_T. The width and height of the cavity are 0.1 and 0.06 cm, respectively. Due to the symmetry along the vertical mid-plane, only half of the cavity needs to be simulated.

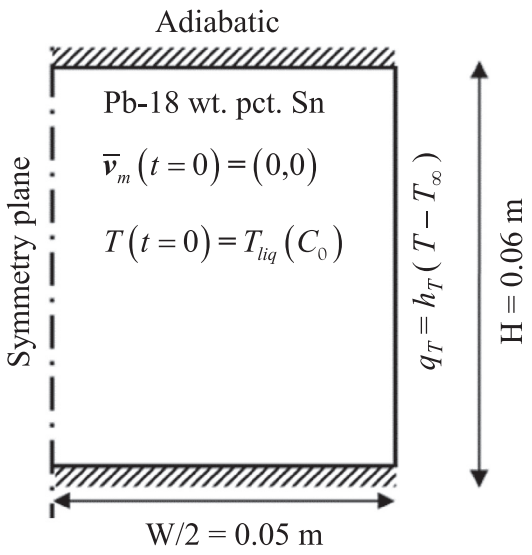

Fig. 2. Schematic of the solidification numerical benchmark problem.

Table 1
Properties of the lead-18 wt. pct. tin alloy.

Property	Unit	Value	Reference
Specific heat	J kg^{-1} K^{-1}	176	[11]
Thermal conductivity	W m^{-1} K^{-1}	17.9	[11]
Reference density	Kg m^{-3}	9250	[11]
Latent heat of fusion	J kg^{-1}	3.76×10^{4}	[11]
Liquid dynamic viscosity	Pa s	1.10×10^{-3}	[11]
Liquid thermal expansion coefficient	K^{-1}	1.16×10^{-4}	[11]
Liquid solutal expansion coefficient	(wt. pct.)$^{-1}$	4.90×10^{-3}	[11]
Melting point at $C = 0$	K	600.65	[11]
Eutectic composition	wt. pct.	61.911	[11]
Eutectic temperature	K	456.15	[11]
Equilibrium partition coefficient	–	0.310	[11]
Liquidus slope	K (wt. pct.)$^{-1}$	−2.334	[11]
Liquidus temperature	K	558.638	[11]
Secondary arm spacing	m	1.85×10^{-4}	[11]
Liquid mass diffusivity	m^{2}s^{-1}	7×10^{-9}	[48,49]
Gibbs–Thomson coefficient	Km	7.9×10^{-8}	[48,49]
Primary arm spacing	m	$2\lambda_2$	[50,51]

4.2. Properties and simulation parameters

The thermophysical and phase diagram properties were taken from Bellet et al. [11]. In addition, the liquid mass diffusivity D_l and the Gibbs–Thomson coefficient Γ, which are required in simulating the three-phase and truncated Scheil models, are equal to $D_l = 7\times10^{-9}\mathrm{m^2s^{-1}}$ and $\Gamma = 7.9\times10^{-8}\mathrm{mK}$ [48,49]. Finally, the primary arm spacing was calculated using $\lambda_1 = 2\lambda_2$ [50,51]. These properties are all summarized in Table 1. From the table, one can see that the thermal and solutal expansion coefficients are both positive. This means that, inside the mush, where the temperatures are lower than the nominal temperature T_{ref} and solute concentrations are higher than the nominal solute concentration C_{ref}, the thermal buoyancy forces will be downward while the solutal buoyancy forces will be upward. Since the value of the solutal expansion coefficient is about forty times larger than the value of the thermal expansion coefficient, the solutal buoyancy forces can be expected to dominate the thermal buoyancy forces.

To verify the numerical results, simulations of the benchmark solidification problem were first performed with a lever-type solidification model. The equations of that model are similar to the equations of the Scheil-type model, and the only difference is that, in the lever-type

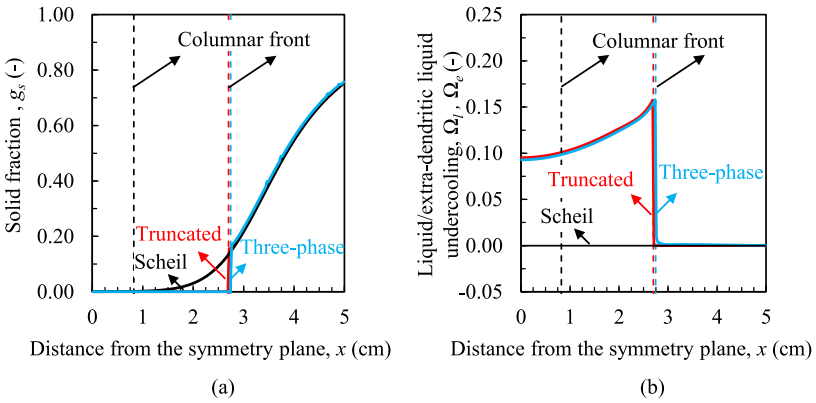

Fig. 3. Comparison between the predictions of the Scheil-type, truncated-Scheil-type, and three-phase models in the absence of melt convection showing profiles of (a) solid fraction and (b) liquid/extra-dendritic liquid undercooling at $t = 60$ s.

model, the equations for the solute balance in the liquid and solid read

$$\left[g_l + k_0(1-g_l)\right]\frac{\partial \bar{C}_l}{\partial t} + \nabla\cdot\left(\boldsymbol{v}\bar{C}_l\right) = \left(1-k_0\right)\bar{C}_l\frac{\partial g_s}{\partial t} \tag{37}$$

and

$$\bar{C}_s = k_0\bar{C}_l \tag{38}$$

respectively. All simulations were performed using a time step $\Delta t = 0.005$ seconds and mesh spacing $\Delta x = \Delta y = 0.25$ millimeters. Simulations were performed on The University of Iowa NEON computer cluster. Using 48 cores, the CPU times for simulating the Scheil-type and truncated-Scheil-type models in the presence of melt convection were about 30 h, while for the three-phase model that time was about 55 h. This indicates that simulating the truncated-Scheil-type model is about two times faster than the three-phase model. Results for the lever-type model were compared with the results in Bellet et al. [11] and excellent agreement was observed for the different quantities.

5. Results and discussion

5.1. No melt convection

In Fig. 3, the comparisons between the predictions of the Scheil-type (the black curves), truncated-Scheil-type (the red curves) and three-phase (the blue curves) models in the absence of melt convection are shown. The curves in the figure show profiles of different quantities along a horizontal line passing through the cavity. Note that disregarding melt convection makes the problem essentially one-dimensional. Fig. 3(a) shows the comparison between the solid fraction profiles at $t = 60$ s; Fig. 3(b) shows the comparison between the liquid undercoolings at that time. The vertical dashed lines show the position of the columnar front predicted by the different models. For the truncated-Scheil-type and three-phase models, as already discussed (see Section 2.6), the columnar front corresponds to the isocontour $\phi = 0$; for the Scheil-type model, the columnar front shown in the figure corresponds to the isocontour $g_s = 0.01$. The choice of 0.01 instead of another small value, for example 0.001, is arbitrary but should not distract because this choice is only for the sake of illustration and has no influence on either the results or the following discussion. First, predictions of the truncated-Scheil-type and Scheil-type models are compared. From Fig. 3(a), it can be seen that the solid fractions predicted by the truncated-Scheil-type model for $x > 2.8$ cm (i.e., behind the columnar front of the truncated-Scheil-type model) are nearly identical to the solid fractions predicted by the Scheil-type model. This is because, as shown in Fig. 3(b), for $x > 2.8$ cm, the liquid undercoolings predicted by these two model models are, as expected (see the discussion below Eq. (26)), equal to zero.

Next, the predictions of the three-phase model shown in Fig. 3(a) and (b) (the blue curves) are analyzed. From Fig. 3(b), one can see that, behind the columnar front (i.e., for $x > 2.8$), the liquid undercoolings predicted by the three-phase model are nearly zero. This is because behind the columnar front, S_{env} has relatively high values (see Eq. (19) and the discussion below and note that λ_1 has a low value in columnar growth). According to Eq. (10), a high value for S_{env} requires $\bar{C}_e \approx \bar{C}_d$, so that the last term in the equation remains finite. That, in turn, and according to Eq. (24) and the fact that $\bar{C}_d = C_l^*$, results in $\Omega_e \approx 0$. Now, if one uses different constitutive relations for $S_{env}$and/or δ_{env}, the predicted values of the different quantities can be expected to be slightly different, but S_{env} will still have a relatively high value behind the front, and therefore Ω_e behind the columnar front will still be nearly zero.

Next, the predictions of the three-phase and truncated-Scheil type models in Fig. 3(a) and (b) are compared. Because the liquid undercoolings behind the front predicted by the three-phase model are nearly zero (see the discussion in the above paragraph), the predictions of that model and the truncated-Scheil-type model (i.e., the predicted columnar front position, solid fractions, and liquid undercoolings) are nearly identical. This is an important observation because it indicates that, for columnar solidification and, at least in the absence of melt convection, one can safely disregard liquid undercooling behind the columnar front and use the truncated-Scheil-type two phase model, instead of the more complex three-phase model.

Next, the accuracy of the conjecture that was proposed in Section 2.7, which stated that by increasing σ^* in the truncated-Scheil-type and three phase models, these models should converge to the Scheil-type model, is examined. In Fig. 4, predictions of the Scheil-type model (the black curve) are compared with the predictions of the truncated-Scheil-type model (the colored curves) with four different values of the tip selection parameter: $\sigma^* = 0.0002$, 0.02, 2.00, and 200. Fig. 4(a) and (b) shows the comparisons between the solid fraction and liquid undercooling profiles, respectively. Results are at $t = 60$ s. It is emphasized that from these four σ^* values, only $\sigma^* = 0.02$ is realistic, and simulations with the three other values are performed only to examine the validity of the conjecture that was proposed in Section 2.7. The vertical lines in the figures show the position of the columnar front. From the plots, it is evident that, in the truncated-Scheil-type model, as the value of σ^* is increased, the length of the undercooled liquid region and the values of liquid undercooling in this region decrease. Finally, with $\sigma^* = 200$, the front positions predicted by the two models nearly collapse. Furthermore, although not shown here for the purpose of concision, the same behavior was observed by increasing σ^* in the three-phase model. These numerical observations confirm our conjecture in Section 2.7: by increasing σ^* in the truncated-Scheil-type and three phase models, these models converge to the Scheil-type model.

One more point regarding Figs. 3 and 4 must be discussed before proceeding. From these figures, it can be seen that when liquid undercooling is taken into account (i.e., in the truncated-Scheil-type and three-phase models with $\sigma^* <= 0.02$), at the position of the columnar front, there is a steep increase in the solid fraction profiles, and the value of

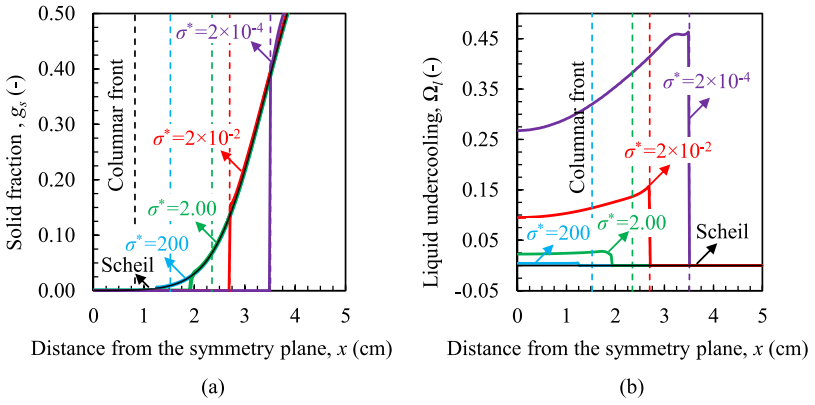

Fig. 4. (a) Solid fraction and (b) liquid undercooling profiles at $t = 60$ s, showing the convergence of the truncated-Scheil-type model to the Scheil-type model as the liquid undercooling vanishes with increase in the tip selection parameter σ^*. Vertical lines show the position of the columnar front.

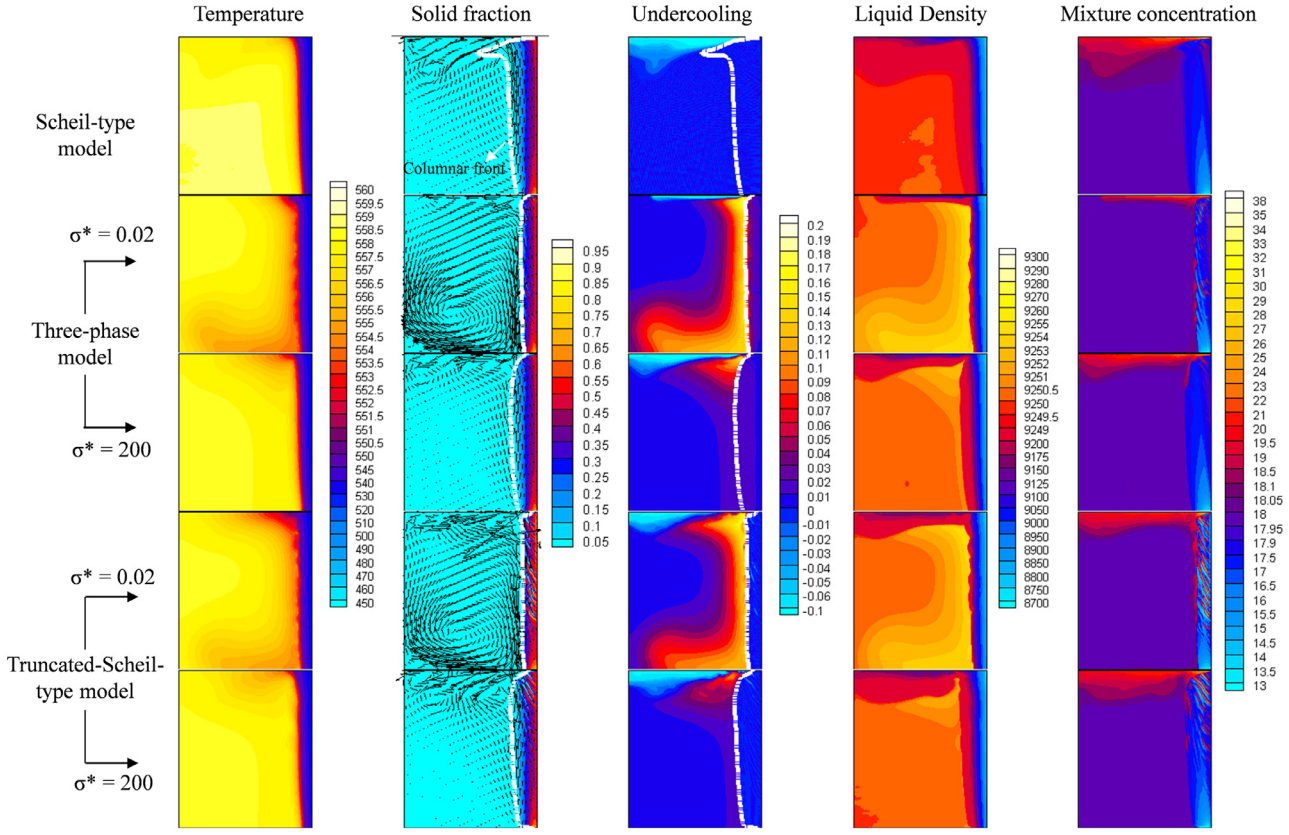

Fig. 5. Snapshots at $t = 10$ s of the different quantities predicted by the Scheil-type, three-phase, and truncated-Scheil-type models. In the second and third columns, the vectors represent the superficial liquid velocity and the white curve represents the columnar front, which corresponds to isoline $g_s = 0.01$ or $\phi = 0$.

the solid fraction immediately behind the columnar front is relatively high (greater than 0.15). This steep increase, which was also observed in the phase-field simulations of Badillo and Beckermann [52], should not be inferred as a discontinuity, and resolving it numerically, especially in the presence of melt convection, requires a relatively fine mesh. When liquid undercooling is disregarded (i.e., the Scheil-type model or truncated-Scheil-type models with $\sigma^* = 200$), however, there is no steep increase in the solid fraction profiles, and the solid fraction immediately behind the columnar front is, as expected, very low. In all the models and for all values of σ^*, the increase in solid fraction behind the columnar front is gradual. In the next subsection, it will be shown that, when melt convection is taken into account, the magnitude of the solid fraction immediately behind the columnar front has a major impact on the flow directions around the front.

5.2. With melt convection

Predictions of the Scheil-type, truncated-Scheil-type, and three-phase models in the presence of melt convection are shown in Figs. 5–7. Fig. 5 shows the results at an early solidification time (i.e., $t = 10$ s) and Figs. 6 and 7 show the results at two intermediate solidification times (i.e., $t = 60$ and 120 s, respectively). The total solidification time was about 550 s. The predictions of the three-phase and truncated-Scheil-type models are shown for two different values of σ^*: $\sigma^* = 0.02$ and $\sigma^* = 200$. It is emphasized again that $\sigma^* = 200$ is unrealistic and simulations with this extremely high value of σ^* are performed only to show how truncated-Scheil-type and three-phase models converge to the Scheil-type model at high σ^* values. The contour plots of the temperature, solid fraction, liquid/extra-dendritic liquid undercooling, liquid

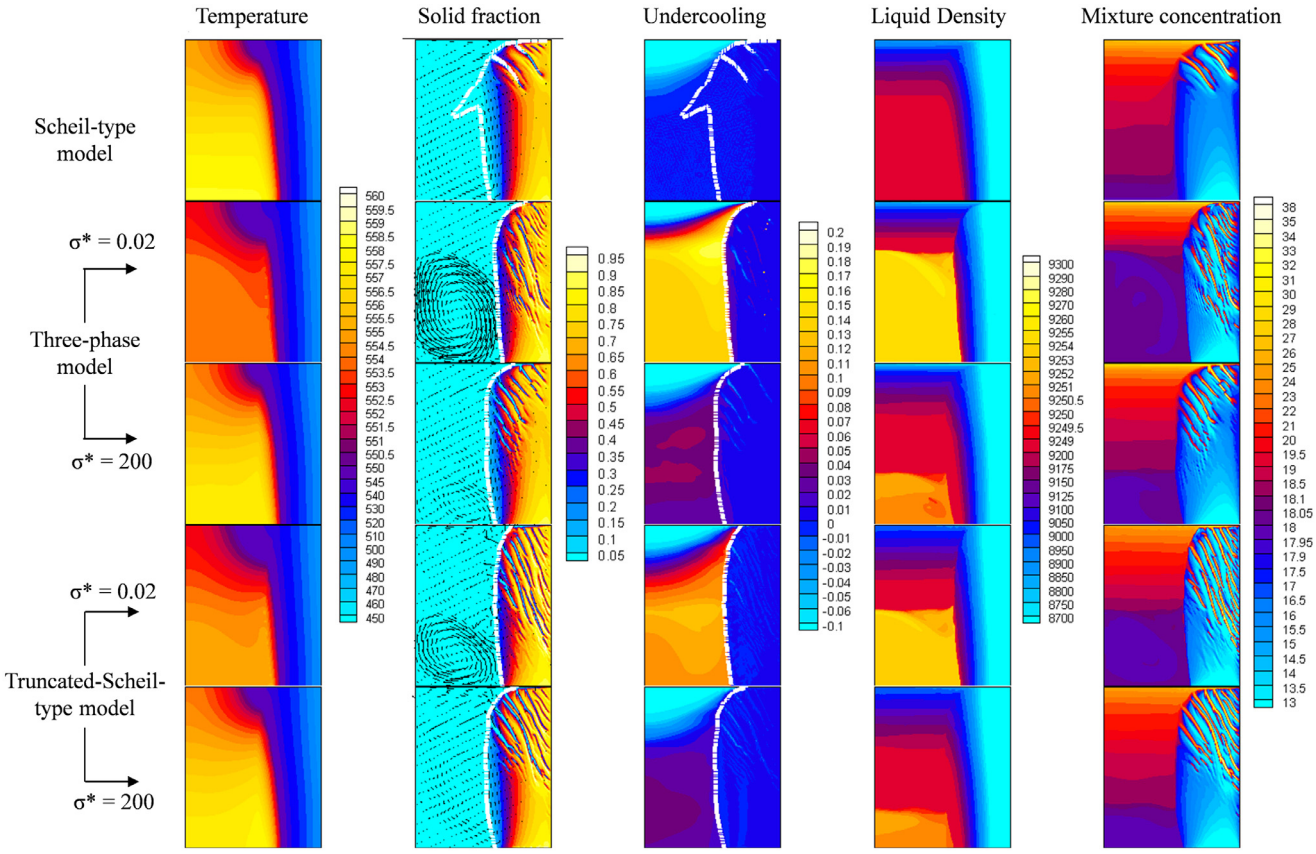

Fig. 6. Snapshots at $t = 60$ s of the different quantities predicted by the Scheil-type, three-phase, and truncated-Scheil-type models. In the second and third columns, the vectors represent the superficial liquid velocity and the white curve represents the columnar front, which corresponds to isoline $g_s = 0.01$ or $\phi = 0$.

density, and mixture concentration are shown in the first through fifth columns, respectively. In the solid fraction contour plots, the vectors and the white curves represent the superficial liquid velocity and the columnar front, respectively. Next, the predictions of the different models are compared.

From the contour plots shown in the second column of these figures, it can be seen that, at $t = 10$ and 60 s, the flow pattern predicted by the different models and at the different values of σ^* are noticeably different. For example, the Scheil-type model predicts that (see the contour plots in the first row second column of Figs. 5 and 6) the strongest melt flow in the simulation domain is the vertical upwards flow behind the columnar front (i.e., at the low solid fraction regions of the mush). This upward flow indicates that the upward solutal buoyancy forces have, as expected (see the discussion at the end of Section 4), dominated the downward thermal buoyancy forces. A similar flow pattern is also predicted by the truncated-Scheil-type and three-phase models with $\sigma^* = 200$ (see the contour plots in the second column, third and fifth rows Fig. 5). However, with $\sigma^* = 0.02$ (see the contour plots in the second column, second and fourth rows), there is no significant melt flow behind the columnar front (except in the channel regions), and the melt flow is mainly ahead of the front. From these observations, one can conclude that in the absence of liquid undercooling (i.e., Scheil-type model and the truncated-Scheil-type and three-phase models with $\sigma^* = 200$), the main flow pattern in the domain is upward flow behind the columnar front; while, in the presence of liquid undercooling (i.e., the truncated-Scheil-type and three-phase models with $\sigma^* = 0.02$), the main flow pattern is downward ahead of the columnar front. It should be mentioned that, because liquid undercooling is present in reality, the flow pattern predicted in the presence of liquid undercooling is expected to be more realistic than the one predicted in the absence of liquid undercooling.

The main reason for the difference that is observed in the flow pattern in the absence and presence of liquid undercooling is the difference in the magnitude of the solid fraction behind the columnar front. From the plots in the second column of Figs. 5 and 6, it can be seen that when liquid undercooling is disregarded (i.e., the Scheil-type model and the three-phase and truncated-Scheil-type models with $\sigma^* = 200$), the solid fractions behind the front are relatively low (less than 0.05); however, when the undercooling is taken into account, these solid fractions have intermediate values (about 0.3). This difference is similar to what was observed when the results without melt convection were discussed (see the discussion at the end of Section 5.1). Low solid fractions behind the columnar front permit relatively strong upward melt flow locally, which leads to a downward flow ahead of the front so that mass continuity is satisfied around the columnar front. When the solid fractions behind the front are not low, the flow behind the front becomes relatively weak and, therefore, cannot influence the flow ahead of the front. As a result, the direction of that flow is determined solely by the downward thermal buoyancy forces.

Next, the liquid undercooling contour plots shown in the third column of Figs. 5–7 are discussed. From the plots, it can be seen that the liquid undercoolings predicted by the Scheil-type model are, as expected (see the discussion below Eq. (26)), zero behind the columnar front. Ahead of the columnar front, these undercoolings are zero in most parts of the cavity, except in a narrow region adjacent to the top wall, where they have negative values. A negative value for liquid undercooling indicates that the liquid is locally superheated: its temperature is above the equilibrium temperature corresponding to the local liquid

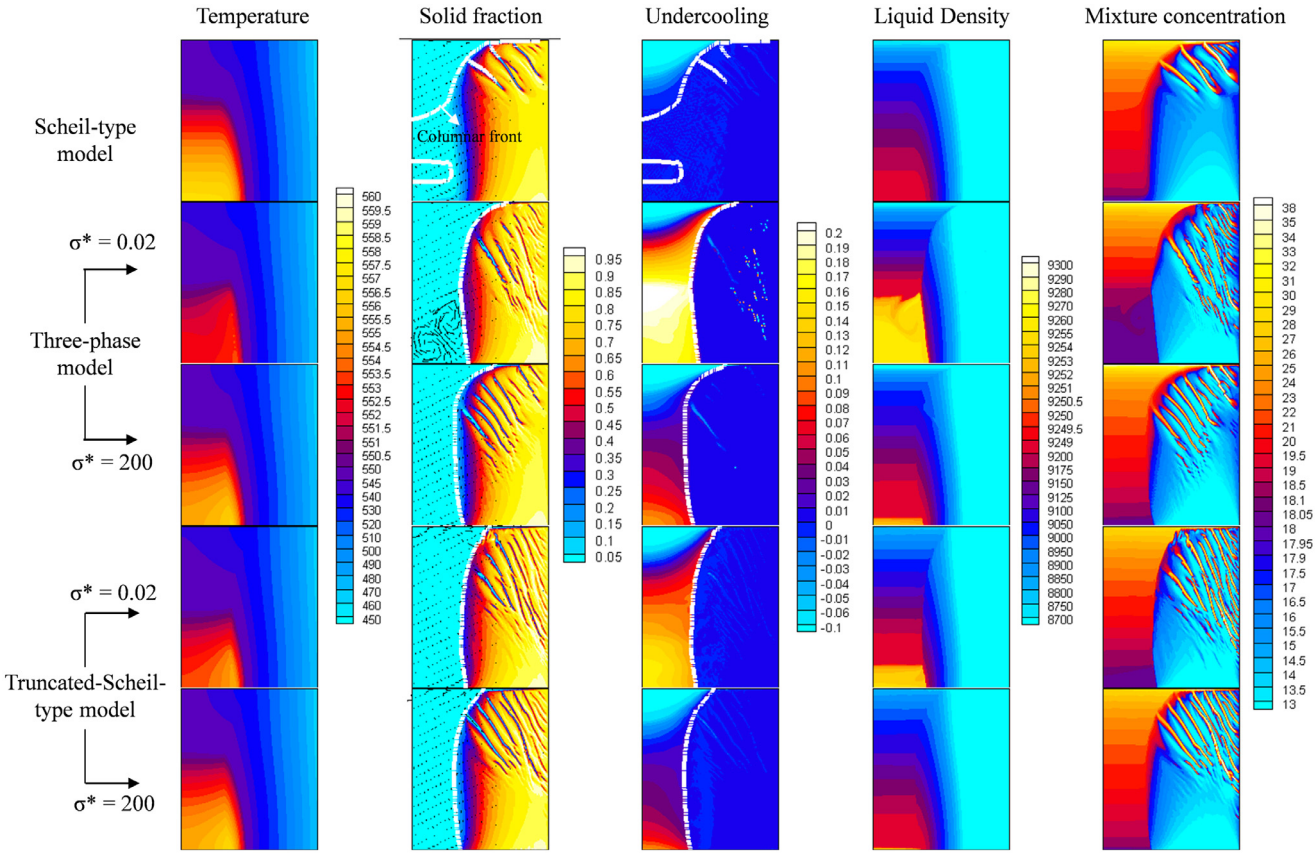

Fig. 7. Snapshots at $t = 120$ s of the different quantities predicted by the Scheil-type, three-phase, and truncated-Scheil-type models. In the second and third columns, the vectors represent the superficial liquid velocity and the white curve represents the columnar front, which corresponds to isoline $g_s = 0.01$ or $\phi = 0$.

concentration. The liquid undercoolings predicted by the truncated-Scheil-type model are, again, as expected, zero behind the columnar front. Ahead of the columnar front, these undercoolings are positive with $\sigma^* = 0.02$, but, with $\sigma^* = 200$, positive liquid undercoolings nearly vanish. The liquid undercoolings predicted by the three-phase model are very similar to the ones predicted by the truncated-Scheil-type model. This indicates that, for columnar solidification, even in the presence of melt convection, the liquid undercooling behind the columnar front can be disregarded and the truncated-Scheil-type model can be used instead of the three-phase model.

From the solid fraction contour plots shown in Figs. 5– 7 it can also be seen that at $t = 60$ s a few channel segregates are fully established (i.e., solid free channels are clearly distinguishable from their neighboring regions, which have relatively high solid fractions). Channels are initiated by convective instabilities in the low solid fraction regions of the semi-solid mush (see [53,54] and references therein). Most metallic alloys, including the lead-tin alloy studied in this paper, have a partition coefficient less than unity; therefore, during their solidification, solute is rejected into the melt. The solute rejection changes the density of the melt and induces buoyancy forces. To understand how channels form, imagine a parcel of highly segregated liquid located deep in the mush. Two types of force act on the parcel: buoyancy forces and frictional forces. If the buoyancy forces acting on the parcel are strong enough to overcome the frictional retarding forces that are exerted by the semi-solid mush, the parcel will move. During that movement, the parcel will retain its composition because its mass diffusivity is much lower than its heat diffusivity. If the local flow velocity and isotherm are misaligned such that the parcel moves towards the low solid fraction regions of the mush, where the temperature is higher, the still highly segregated, displaced parcel will delay solidification or even locally re-melt the solid. That will increase the local permeability of the mush. The local increase in the permeability allows the subsequent parcels to flow more easily. This, in turn, delays solidification (or enhances re-melting) even further until open channels form that are completely free of solid.

It is also interesting to note that in different models channels start to appear at different heights of the cavity. In the Scheil-type model, channels appear only in the top one-third of the cavity around the top right corner. This is because at lower heights of the cavity the local isotherms and flow direction are both nearly vertical. Around that corner, however, the flow starts to turn left and therefore makes an angle with respect to the isotherms that are still nearly vertical. Since misalignment between the local flow direction and isotherms is necessary for channels to form, they form only around the top right corner. In the three-phase and truncated-Scheil-type models, however, channels are observed also at lower heights and even close to the bottom of the cavity. Formation of channels at such low heights indicates that in the three-phase and truncated-Scheil-type models, the local flow direction and the isotherms become misaligned not only at the top right corner but also at lower heights.

In Fig. 8, the final macrosegregation patterns (i.e., the final distribution of the mixture concentration C) predicted by the three models are shown. Again, results for the three-phase and truncated-Scheil-type models are shown for $\sigma^* = 0.02$ and 200. First, the macrosegregation pattern predicted by the Scheil model, and shown in contour plot 8(a), is analyzed. To more easily discuss the pattern in the plot, four different regions, enclosed by the closed curves which are numbered one to four, are identified in the plot. Next, the segregation patterns in these regions are discussed. Region one is negatively segregated (i.e., it has $C < C_0$) because during solidification of this part of the cavity, the local melt flow is relatively strong and, therefore, it carries away the solute that is

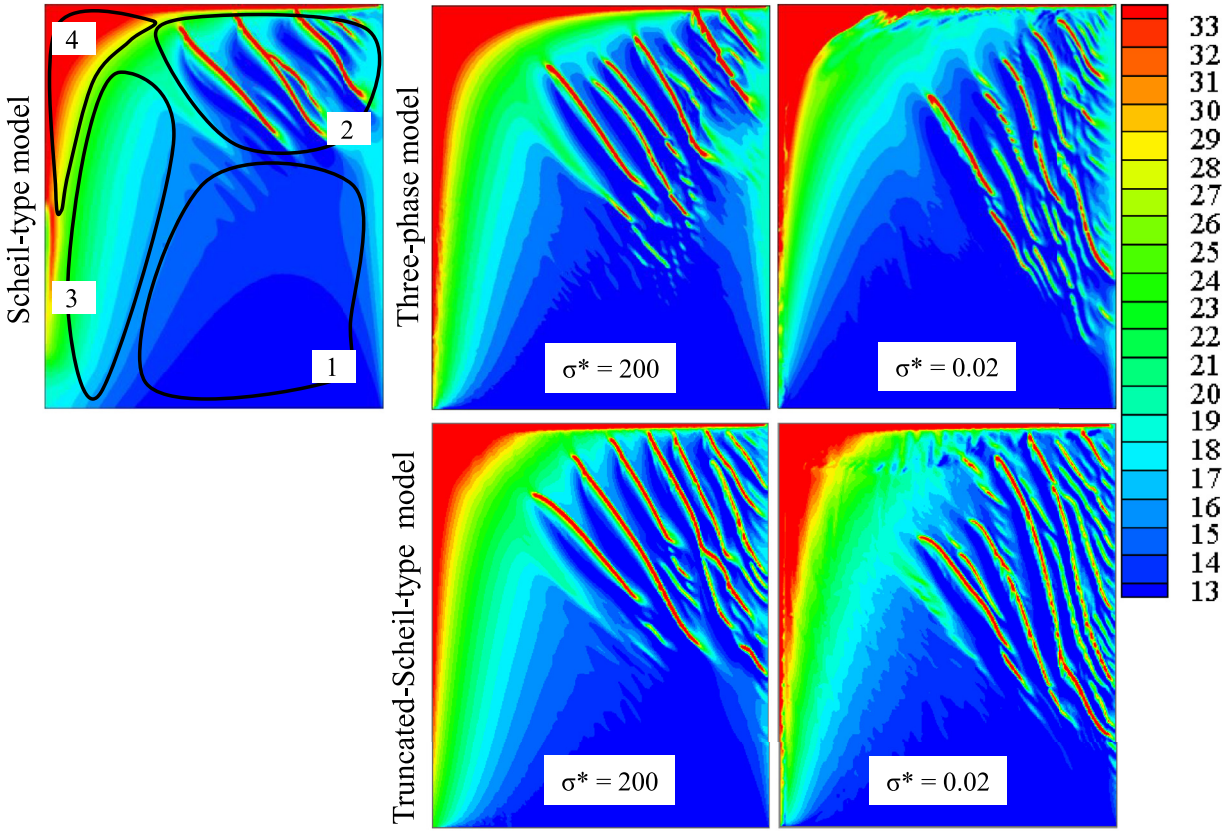

Fig. 8. Final macrosegregation maps predicted by the Scheil-type, three-phase, and truncated-Scheil-type models.

rejected locally during solidification. In region two, macrosegregation is dominated by the formation of three highly segregated channels, which are separated from each other by regions of very low segregation. Region three has solute concentrations that are nearly equal to the nominal solute composition C_{ref}; in other words, there is no significant solute segregation in this region. This is because, during solidification of region three, the local melt flow is relatively weak (as that region solidifies only after about three quarters of the cavity has been already occupied by the mush). Region four has solute concentrations much higher than C_{ref} (i.e., it is highly segregated) because when highly segregated, and therefore relatively light, liquid parcels reach that region of the cavity, they stay there and do not move to the other parts of the cavity anymore.

By examining the other plots in Fig. 8, one can see that the three-phase and truncated-Scheil-type models predict overall macrosegregation patterns, which is a term used to refer to segregation patterns excluding channel segregates, that are very similar to the pattern predicted by the Scheil-type model. In other words, accounting for liquid undercooling has no significant influence on the overall macrosegregation pattern. This is because, regardless of whether liquid undercooling is taken into account or not, regions one and three solidify in the presence and absence of strong local melt flow, respectively; region four is the region where light and highly segregated liquid parcels accumulate. Therefore, regions one and four always exhibit negative and highly positive macrosegregation, respectively, while region three solidifies with no significant macrosegregation. The only major difference that is observed between the segregation patterns predicted by the different models and/or the different values of σ^* is the form of the predicted channel segregates. In other words, accounting for liquid undercooling changes the form of the predicted channel segregates but not the overall macrosegregation pattern. The difference in the form of the channel segregates is attributed to the difference in the flow pattern around the columnar front during solidification, which was discussed in connection with Fig. 5. It is emphasized that, although it was shown here that liquid undercooling has no significant impact on the final macrosegregation pattern, accounting for it in solidification models remains critical because some important phenomena, such as nucleation of equiaxed grains, can be predicted only if liquid undercooling is accounted for.

6. Conclusions

A truncated-Scheil-type two-phase model was developed for columnar solidification of binary alloys in the presence of melt convection and liquid undercooling ahead of the columnar front. The model was derived from a three-phase columnar solidification model, which takes into account liquid undercooling both ahead and behind the columnar front. A fast and robust numerical scheme to calculate solid fractions during solidification was developed. A key advantage of the scheme, compared to similar schemes that are available in the literature, is that its implementation in the open-source widely-used CFD package OpenFOAM does not require parallel-specific programming. This allowed us to perform high-resolution simulations where channel segregates are fully resolved. In addition, for the first time in the field of macroscale modeling of solidification, complex movements of the columnar front in the presence of melt convection, liquid undercooling, and channel segregates were tracked.

These models were used to perform simulations of a numerical columnar solidification benchmark problem, and the results were compared with the predictions of a Scheil-type model, which neglects liquid undercooling entirely. It was found that the predictions of the truncated-Scheil-type model and the three-phase model are nearly identical. This indicates that, for columnar solidification, the truncated-Scheil-type model can be used instead of the more complex three-phase model.

It was also found that, in the truncated-Scheil-type and three-phase models, the dendrite tip selection parameter σ^* is a key parameter. With the realistic value of σ^* (i.e., $\sigma^* = 0.02$), these models account for liquid undercooling; as the value of σ^* is increased, the predicted liquid undercooling vanishes and the predictions of these models converge to the predictions of the Scheil-type model. It was also found that accounting for liquid undercooling had no significant impact on the final macrosegregation patterns but changed the flow pattern around the primary tips during solidification as well as the form of the channel segregates. It is emphasized that liquid undercooling is nonetheless very important to account for because some important phenomena, such as nucleation of equiaxed grains, can be predicted only if liquid undercooling is taken into account.

Future work will include incorporating equiaxed growth so that the columnar to equiaxed transition can be predicted. It would also be interesting to use the three-phase and truncated-Scheil-type models to perform three-dimensional simulations of the numerical benchmark problem and investigate the effect of liquid undercooling on the shape of the channel segregates in 3D.

Acknowledgments

This work was financially supported by NASA (NNX14AD69G).

Declaration of interest

No conflict of interest.

References

[1] C. Beckermann, R. Viskanta, Double-diffusive convection during dendritic solidification of a binary mixture, Phys. Chem. Hydrodyn. 10 (1988) 195–213.
[2] C. Beckermann, R. Viskanta, Mathematical modeling of transport phenomena during alloy solidification, Appl. Mech. Rev. 46 (1993) 1–27.
[3] W.D. Bennon, F.P. Incropera, A continuum model for momentum, heat and species transport in binary solid-liquid phase change systems-I. Model formulation, Int. J. Heat Mass Transf. 30 (10) (1987) 2161–2170.
[4] W.D. Bennon, F.P. Incropera, A continuum model for momentum, heat and species transport in binary solid-liquid phase change systems-II. Application to solidification in a rectangular cavity, Int. J. Heat Mass Transf. (1987).
[5] C. Beckermann, Modelling of macrosegregation: applications and future needs, Int. Mater. Rev. 47 (5) (2002) 243–261.
[6] A. Ludwig, M. Wu, A. Kharicha, On macrosegregation, Metall. Mater. Trans. A 46 (11) (2015) 4854–4867.
[7] T. Carozzani, C.-A. Gandin, H. Digonnet, M. Bellet, K. Zaidat, Y. Fautrelle, Direct simulation of a solidification benchmark experiment, Metall. Mater. Trans. A 44 (2) (2013) 873–887.
[8] A. Saad, C.-A. Gandin, M. Bellet, N. Shevchenko, S. Eckert, Simulation of channel Segregation during directional solidification of In—75 wt pct Ga. qualitative comparison with in situ observations, Metall. Mater. Trans. A 46 (11) (2015) 4886–4897.
[9] A. Kumar, B. Dussoubs, M. Založnik, H. Combeau, Effect of discretization of permeability term and mesh size on macro-and meso-segregation predictions, J. Phys. D. Appl. Phys. 42 (10) (2009) 105503.
[10] A. Kumar, M. Založnik, H. Combeau, B. Goyeau, D. Gobin, A numerical simulation of columnar solidification: influence of inertia on channel segregation, Model. Simul. Mater. Sci. Eng. 21 (4) (2013).
[11] M. Bellet, et al., Call for contributions to a numerical benchmark problem for 2D columnar solidification of binary alloys, Int. J. Therm. Sci. 48 (11) (2009) 2013–2016.
[12] H. Combeau, et al., Analysis of a numerical benchmark for columnar solidification of binary alloys, IOP Conf. Ser. Mater. Sci. Eng. 33 (1) (2012).
[13] S.C. Flood, J.D. Hunt, A model of a casting, Math. Comput. Model. 10 (10) (1988) 795.
[14] C.Y. Wang, C. Beckermann, A multiphase solute diffusion model for dendritic alloy solidification, Metall. Trans. A 24 (12) (1993) 2787–2802.
[15] C.Y. Wang, C. Beckermann, Equiaxed dendritic solidification with convection: part I. Multiscale/multiphase modeling, Metall. Mater. Trans. A Phys. Metall. Mater. Sci. 27 (9) (1996) 2754–2764.
[16] C.Y. Wang, C. Beckermann, Equiaxed dendritic solidification with convection: part II. Numerical simulations for an AI-4 Wt Pct Cu alloy, Metall. Mater. Trans. A Phys. Metall. Mater. Sci. 27 (9) (1996) 2765–2783.
[17] C. Beckermann, C.Y. Wang, Equiaxed dendritic solidification with convection" Part III. comparisons with NH4CI-H20 experiments, Am. J. Physiol. 240 (1981) H868–H873.
[18] C.Y. Wang, C. Beckermann, Prediction of columnar to equiaxed transition during diffusion-controlled dendritic alloy solidification, Metall. Mater. Trans. A 25 (5) (1994) 1081–1093.
[19] M.A. Martorano, C. Beckermann, C.A. Gandin, A solutal interaction mechanism for the columnar-to-equiaxed transition in alloy solidification, Metall. Mater. Trans. A Phys. Metall. Mater. Sci. 34 (8) (2003) 1657–1674 A.
[20] M. Založnik, H. Combeau, Thermosolutal flow in steel ingots and the formation of mesosegregates, Int. J. Therm. Sci. 49 (9) (2010) 1500–1509.
[21] H. Combeau, M. Založnik, M. Bedel, Predictive capabilities of multiphysics and multiscale models in modeling solidification of steel ingots and DC casting of aluminum, JOM 68 (8) (2016) 2198–2206.
[22] A. Pakanati, M. M'Hamdi, H. Combeau, M. Založnik, Investigation of macrosegregation formation in aluminium DC casting for different alloy systems, Metall. Mater. Trans. A Phys. Metall. Mater. Sci. 49 (10) (2018) 4710–4721.
[23] A. Pakanati, K.O. Tveito, M. M'Hamdi, H. Combeau, M. Založnik, Application of an equiaxed grain growth and transport model to study macrosegregation in a DC casting experiment, Metall. Mater. Trans. A 50 (4) (2019) 1773–1786.
[24] T. Koshikawa, M. Bellet, C.A. Gandin, H. Yamamura, M. Bobadilla, Experimental study and two-phase numerical modeling of macrosegregation induced by solid deformation during punch pressing of solidifying steel ingots, Acta Mater. 124 (2017) 513–527.
[25] T.T.M. Nguyen, C.A. Gandin, H. Combeau, M. Založnik, M. Bellet, Finite element multi-scale modeling of chemical segregation in steel solidification taking into account the transport of equiaxed grains, Metall. Mater. Trans. A Phys. Metall. Mater. Sci. 49 (5) (2018) 1725–1748.
[26] M. Torabi Rad, C. Beckermann, Validation of a model for the columnar to equiaxed transition with melt convection, Miner. Met. Mater. Ser. Part F2 (2016) 85–92.
[27] J. Guo, C. Beckermann, Three-dimensional simulation of freckle formation during binary alloy solidification: effect of mesh spacing, Numer. Heat Transf. Part A Appl. 44 (6) (2003) 559–576.
[28] A. Kumar, M. Založnik, H. Combeau, Study of the influence of mushy zone permeability laws on macro- and meso-segregations predictions, Int. J. Therm. Sci. 54 (2012) 33–47.
[29] M. Torabi Rad, M. Založnik, H. Combeaub, C. Beckermann, Upscaling mesoscopic simulation results to develop constitutive relations for macroscopic modeling of equiaxed dendritic solidification, Materialia 5 (2019) 100231.
[30] S. McFadden, et al., Validation of a front-tracking model of the columnar to equiaxed transition using solidification results from the Maxus 7 microgravity platform, J. Jpn. Soc. Microgravity Appl. 25 (3) (2008) 489 484.
[31] M. Rebow, D.J. Browne, Y. Fautrelle, Combined analytical and numerical front tracking approach to modeling directional solidification of a TiAl-based intermetallic alloy for design of microgravity experiments, Mater. Sci. Forum 649 (2010) 243–248.
[32] W. Mirihanage, S. McFadden, D.J. Browne, Macroscopic model for predicting columnar to equiaxed transitions using columnar front tracking and average equiaxed growth, Mater. Sci. Forum 649 (2010) 355–360.
[33] R.P. Mooney, S. McFadden, M. Rebow, D.J. Browne, A front tracking model for transient solidification of Al-7wt%Si in a Bridgman furnace, Trans. Indian Inst. Met. 65 (6) (2012) 527–530.
[34] D.J. Browne, J.D. Hunt, An interface-tracking model of moving boundaries in multi--phase systems: application to solidification, Arch. Thermodyn. 24 (1) (2003) 25–36.
[35] D.J. Browne, J.D. Hunt, A fixed grid front-tracking model of the growth of a columnar front and an equiaxed grain during solidification of an alloy, Numer. Heat Transf. Part B Fundam. 45 (5) (2004) 395–419.
[36] S. McFadden, D.J. Browne, J. Banaszek, Prediction of the formation of an equiaxed zone ahead of a columnar front in binary alloy castings: indirect and direct methods, Mater. Sci. Forum 508 (2009) 325–330.
[37] S. McFadden, D.J. Browne, A front-tracking model to predict solidification macrostructures and columnar to equiaxed transitions in alloy castings, Appl. Math. Model. 33 (3) (2009) 1397–1416.
[38] D.J. Browne, A new equiaxed solidification predictor from a model of columnar growth, ISIJ Int. 45 (1) (2006) 37–44.
[39] J. Banaszek, D.J. Browne, Modelling columnar dendritic growth into an undercooled metallic melt in the presence of convection, Mater. Trans. 46 (6) (2005) 1378–1387.
[40] J. Banaszek, S. McFadden, D.J. Browne, L. Sturz, G. Zimmermann, Natural convection and columnar-to-equiaxed transition prediction in a front-tracking model of alloy solidification, Metall. Mater. Trans. A Phys. Metall. Mater. Sci. 38A (7) (2007) 1476–1484.
[41] M. Seredynski, J. Banaszek, Front tracking based macroscopic modeling of equiaxed and columnar zones in a binary alloy solidification, J. Power Technol. 91 (2) (2011) 77–81.
[42] J. Banaszek, M. Seredynski, The accuracy of a solid packing fraction model in recognizing zones of different dendritic structures, Int. J. Heat Mass Transf. 55 (15–16) (2012) 4334–4339.
[43] Y. Sun, C. Beckermann, Sharp interface tracking using the phase-field equation, J. Comput. Phys. 220 (2) (2007) 626–653.
[44] J.A. Dantzig, M. Rappaz, Solidification, EPFL press, 2009.
[45] H. Jasak, Error Analysis and Estimation for the Finite Volume Method with Applications to Fluid Flows, Imperial College of Science, Technology and Medicine, 1996.
[46] H. Jasak, A. Jemcov, Z. Tukovic, OpenFOAM: a C++ library for complex physics simulations, in: International Workshop on Coupled Methods in Numerical Dynamics, 2007, pp. 1–20.
[47] T. Aslam, A partial differential equation approach to multidimensional extrapolation, in: Proceedings of the - International Conference on Image Processing ICIP, 1, 2004, pp. 649–652.
[48] E. Cadirli, M. Gündüz, The directional solidification of Pb-Sn alloys, J. Mater. Sci. 35 (15) (2000) 3837–3848.

[49] M. Gündüz, J.D. Hunt, The measurement of solid-liquid surface energies in the Al–Cu, Al–Si and Pb–Sn systems, Acta Metall. 33 (9) (1985) 1651–1672.
[50] M. Imagumbai, Relationship between primary- and secondary-dendrite arm spacing of C–Mn steel uni-directionally solidified in steady state, ISIJ Int. 34 (12) (1994) 986–991.
[51] M. Imagumbai, Behaviors of manganese–sulfide in aluminum-killed steel solidified uni-directionally in steady state dendrite structure and inclusions, ISIJ Int. 34 (1 994) (1994) 896–905.
[52] A. Badillo, C. Beckermann, Phase-field simulation of the columnar-to-equiaxed transition in alloy solidification, Acta Mater. 54 (8) (2006) 2015–2026.
[53] M. Torabi Rad, P. Kotas, C. Beckermann, Rayleigh number criterion for formation of A-segregates in steel castings and ingots, Metall. Mater. Trans. A Phys. Metall. Mater. Sci. 44 (9) (2013) 4266–4281.
[54] M. Torabi Rad, Multiphase Macroscale Models for Macrosegregation and Columnar to Equiaxed Transition During Alloy Solidification, The University of Iowa, 2018.